J. Fluid Mech. (2018), *vol.* 850, *pp.* 120–155. © Cambridge University Press 2018
doi:10.1017/jfm.2018.466

Direct numerical simulation of wind turbulence over breaking waves

Zixuan Yang[1], Bing-Qing Deng[1] and Lian Shen[1,†]

[1]Department of Mechanical Engineering and St. Anthony Falls Laboratory, University of Minnesota, Minneapolis, MN 55455, USA

(Received 13 March 2018; revised 12 May 2018; accepted 27 May 2018; first published online 4 July 2018)

We study wind turbulence over breaking waves based on direct numerical simulation (DNS) of two-fluid flows. In the DNS, the air and water are simulated as a coherent system, with the interface captured using the coupled level-set and volume-of-fluid method. Because the wave breaking is an unsteady process, we use ensemble averaging over 100 runs to define turbulence statistics. We focus on analysing the turbulence statistics of the airflow over breaking waves. The effects of wave age and wave steepness are investigated. It is found that before wave breaking, the turbulence statistics are largely influenced by the wave age. The vertical gradient of mean streamwise velocity is positive at small and intermediate wave ages, but it becomes negative near the wave surface at large wave age as the pressure force changes from drag to thrust. Furthermore, wave-coherent motions make increasingly important contributions to the momentum flux and kinetic energy of velocity fluctuations (KE-F) as the wave age increases. During the wave breaking process, spilling breakers do not influence the wind field significantly; in contrast, plunging breakers alter the structures of wind turbulence near the wave surface drastically. It is observed from the DNS results that during wave plunging, a high pressure region occurs ahead of the wave front, which further accelerates the wind in the downstream direction. Meanwhile, a large spanwise vortex is generated, which greatly disturbs the airflow around it, resulting in large magnitudes of Reynolds stress and turbulence kinetic energy (TKE) below the wave crest. Above the crest, the magnitude of KE-F is enhanced during wave plunging at small and large wave ages, but at intermediate wave age, the transient enhancement of KE-F is absent. The effect of wave breaking on the magnitude of KE-F is further investigated through the analysis of the KE-F production. It is discovered that at small wave age, the transient enhancement of KE-F is caused by the appearance of a local maximum in the profile of total momentum flux; but at large wave age, it results from the change in the sign of the KE-F production from negative to positive, due to the sign change in the wave-coherent momentum flux. At intermediate wave age, neither of these two processes is present, and the transient growth of KE-F does not take place.

Key words: air/sea interactions, turbulence simulation, wave breaking

† Email address for correspondence: shen@umn.edu

https://doi.org/10.1017/jfm.2018.466 Published online by Cambridge University Press

1. Introduction

The interactions between wind and water waves influence the sea states, marine atmospheric boundary layer and upper-ocean dynamics. Strong wind forcing leads to wave breaking in oceans, which plays an important role in air–sea interactions. As summarized in many review papers (see for example, Banner & Peregrine 1993; Melville 1996; Perlin & Schultz 2000; Duncan 2001; Kiger & Duncan 2012; Perlin, Choi & Tian 2013), wave breaking limits the amplitude of surface waves, generates ocean currents, vorticity and turbulence and enhances the transport of mass, momentum and energy between the atmosphere and oceans. The investigation of wind over breaking waves is helpful for the development of ocean–atmosphere interaction models.

Extensive field measurements, laboratory experiments and numerical simulations have been conducted to study breaking waves. The previous studies covered various aspects of the flow physics, including the instability mechanisms leading to wave breaking (e.g. McLean *et al.* 1982; Melville 1982; Su *et al.* 1982; Longuet-Higgins & Tanaka 1997*a*,*b*), geometrical properties of breaking waves (e.g. Duncan 1981, 1983; Longuet-Higgins 1982; New 1983; Bonmarin 1989; Skyner 1996; Chang & Liu 1998; Duncan *et al.* 1999; Melville, Veron & White 2002; Wu & Yao 2004; Diorio, Liu & Duncan 2009; Babanin *et al.* 2010), onset criteria for wave breaking (e.g. Duncan 1983; Bonmarin & Ramamonjiarisoa 1985; Rapp & Melville 1990; Schultz, Huh & Griffin 1994; Perlin, He & Bernal 1996; Banner & Tian 1998; Johannessen & Swan 2001; Qiao & Duncan 2001; Song & Banner 2002; Stansell & MacFarlane 2002; Wu & Nepf 2002; Yao & Wu 2005; Babanin *et al.* 2007; Chiang & Hwung 2007; Kharif *et al.* 2008; Tian, Perlin & Choi 2008; Toffoli *et al.* 2010), mechanisms of air entrainment (e.g. Lamarre & Melville 1991; Deane & Stokes 2002; Blenkinsopp & Chaplin 2007; Wang, Yang & Stern 2016), capillary effects (e.g. Longuet-Higgins 1992; Perlin, Lin & Ting 1993; Zhang 1995; Fedorov, Melville & Rozenberg 1998; Jiang *et al.* 1999; Deike, Popinet & Melville 2015) and transport of momentum and energy (e.g. Rapp & Melville 1990; Nepf, Wu & Chan 1998; Tulin & Waseda 1999; Meza, Zhang & Seymour 2000; Yao & Wu 2004; Banner & Peirson 2007; Drazen, Melville & Lenain 2008; Iafrati 2009; Tian, Perlin & Choi 2010; Babanin 2011).

Many laboratory experiments have been conducted to study the wind field over breaking waves. Banner & Melville (1976) discovered that the onset of wave breaking is accompanied by airflow separation. Their analysis was based on steady wave breakers, which are nearly stationary in the coordinate fixed to the waves. Kawai (1982) and Kawamura & Toba (1988) investigated wind over unsteady breaking waves. They observed airflow separation from the wave crest. Reul, Branger & Giovanangeli (1999) further measured the flow field in the region extending to the vicinity of the air–water interface. They found that the geometry of the breaking front resembles a backward-facing step, and crest-to-crest airflow separation takes place over a chain of breaking waves. Although airflow separation can also take place over non-breaking waves (Weissman 1986), Reul, Branger & Giovanangeli (2008) pointed out that the separation induced by breaking waves is stronger and more consistent. Buckley & Veron (2016) studied wind over waves with a range of wave ages, defined as the ratio of the wave phase speed to the characteristic velocity of wind. They reported that the airflow separation happens at small wave ages but is absent at large wave ages.

The airflow separation influences the transport of momentum between air and water. Banner & Melville (1976) showed that the drag force exerted on the wind is significantly larger over breaking waves than over non-breaking waves. Banner (1990) attributed the high drag of wind over breaking waves to the pressure minimum and

https://doi.org/10.1017/jfm.2018.466 Published online by Cambridge University Press

maximum occurring on the leeward and windward of the wave crest, respectively. Banner & Peirson (1998) and Belcher & Hunt (1998) pointed out that the significant increase of the pressure drag with the wave steepness is responsible for the high total drag of wind over breaking waves. By assuming that the wave surface forms a backward-facing step during wave breaking, Kudryavtsev & Makin (2001) proposed a wind–wave coupled model to account for the form drag augment related to wave breaking.

It was discovered in many field measurements (Powell, Vickery & Reinhold 2003; Jarosz *et al.* 2007; Bell, Montgomery & Emanuel 2012; Holthuijsen, Powell & Pietrzak 2012; Zhao *et al.* 2015), laboratory experiments (Donelan *et al.* 2004; Takagaki *et al.* 2012; Troitskaya *et al.* 2012), and numerical simulations based on wind–wave coupled models (Moon, Ginis & Hara 2004; Kudryavtsev & Makin 2007; Mueller & Veron 2009; Liu, Guan & Xie 2012) that the drag coefficient saturates at high wind speeds. New interests were then drawn to the research of wind during wave breaking, wherein the airflow separation over the wave crest is regarded as one of the possible physical processes leading to the saturation of the drag coefficient. Veron, Saxena & Misra (2007) measured the flow field inside the viscous sublayer over wind-generated breaking waves to study the along-surface viscous shear stress. They observed that due to the airflow separation, there is a drastic drop of the surface tangential stress near the wave trough. Reul *et al.* (2008) conducted experiments to study the airflow separation over mechanically generated breaking waves. They showed that the separation layer becomes higher as the wave steepness increases, and the surface tangential stress is low inside the separation bubble.

To date, most understandings of the physics of wind over breaking waves have come from laboratory experiments and field measurements. As an important complementary research tool to experiments, numerical simulations are able to provide details of the flow field. Although numerical simulations have been used to study wave breaking (Chen *et al.* 1999; Song & Sirviente 2004; Iafrati 2009, 2011; Tian, Perlin & Choi 2012; Iafrati, Babanin & Onorato 2013; Derakhti & Kirby 2014; Deike *et al.* 2015; Lubin & Glockner 2015; Deike, Melville & Popinet 2016; Derakhti & Kirby 2016; Pizzo, Deike & Melville 2016), much less attention was paid to the wind turbulence over breaking waves.

The numerical methods for simulating flows with a wave surface can be categorized into one-fluid and two-fluid simulations. The one-fluid simulation has been successfully used to study airflow over prescribed non-breaking waves (see e.g. Sullivan, McWilliams & Moeng 2000; Yang & Shen 2010; Druzhinin, Troitskaya & Zilitinkevich 2012; Sullivan, McWilliams & Patton 2014; Hara & Sullivan 2015). To study the effect of wave breaking on wind turbulence using one-fluid simulations, Suzuki, Hara & Sullivan (2015) modelled the impact of wave breaking events by adding localized form drag. Sullivan *et al.* (2018) extended the application of one-fluid simulations to the investigation of wind over steady breaking waves and unsteady steep waves, wherein the waves act as a bottom boundary with prescribed motions obtained from potential flow theory or measurements. In two-fluid simulations, the air and water are treated as a coherent system. The two-fluid simulation needs an interface-capturing technique, which includes but is not limited to the level-set (LS) method (e.g. Osher & Sethian 1988; Sussman, Smereka & Osher 1994; Sussman *et al.* 1998), volume-of-fluid (VOF) method (e.g. Scardovelli & Zaleski 1999; López *et al.* 2005; Weymouth & Yue 2010) and coupled LS and VOF (CLSVOF) method (e.g. Sussman & Puckett 2000; Liu 2012). In general, the VOF method has good performance in conserving the mass of each phase of the fluids, while the LS method can capture the geometry of waves accurately.

https://doi.org/10.1017/jfm.2018.466 Published online by Cambridge University Press

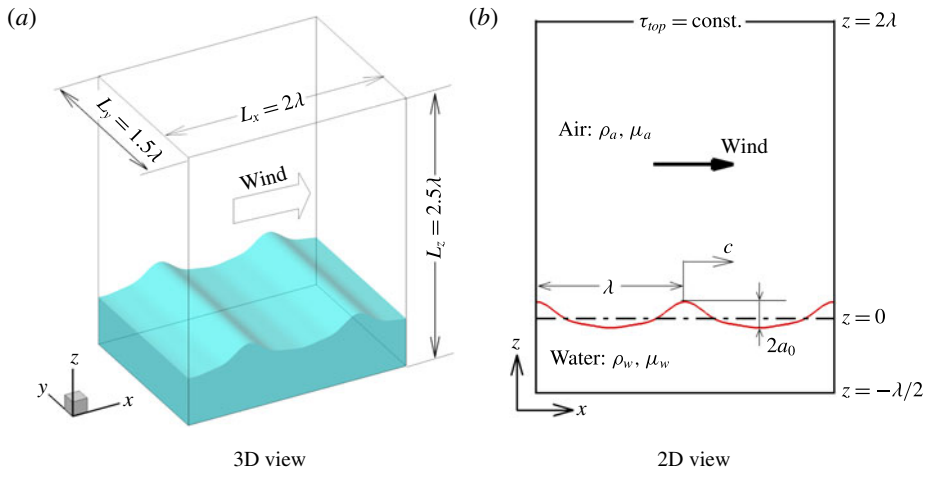


FIGURE 1. (Colour online) Computational domain and coordinate system for DNS of wind over steep and breaking waves.

Although the numerical method for the two-fluid simulation is relatively mature, it is challenging to conduct fine-resolution simulations of breaking waves due to the high computational cost. Previously, two-dimensional (2-D) simulations were performed to describe the general process of wave breaking (Chen *et al.* 1999; Song & Sirviente 2004), study the energy dissipation (Chen *et al.* 1999; Iafrati 2009, 2011), investigate the effects of surface tension (Song & Sirviente 2004; Deike *et al.* 2015) and wave steepness (Iafrati 2009; Deike *et al.* 2015) and analyse the influence of wave breaking on the initially stationary air (Iafrati *et al.* 2013). However, 2-D simulations cannot capture turbulence without using turbulent models. In this sense, three-dimensional (3-D) simulations are desired to study the dynamics of wind turbulence over breaking waves.

In the present study, we perform direct numerical simulations (DNS) of turbulent wind over breaking waves with the breaking process explicitly resolved. The air–water interfaces are captured using the CLSVOF method. The objective is to study the effect of wave breaking on the momentum and energy transfer in the airflow. The effects of wave age and wave steepness are analysed. The remainder of this paper is organized as follows: in § 2, the numerical algorithms are introduced; in § 3, the simulation parameters are described; in § 4, the results are analysed, including mean velocity, cross-surface momentum flux, Reynolds stress and turbulence kinetic energy; in § 5, major conclusions are summarized.

2. Governing equations and numerical algorithms

Figure 1 shows the computational domain and coordinates used in the present simulations. Let x, y and z (or x_1, x_2 and x_3) denote respectively the streamwise, spanwise and vertical directions, with the corresponding velocity components represented by u, v and w (or u_1, u_2 and u_3), respectively. The air and water are treated as a coherent system with the density and viscosity varying with the fluid phase. The flows of air and water are governed by the following continuity and momentum equations:

$$\frac{\partial u_i}{\partial x_i} = 0, \tag{2.1}$$

https://doi.org/10.1017/jfm.2018.466 Published online by Cambridge University Press

$$\rho(\phi)\left(\frac{\partial u_i}{\partial t}+u_j\frac{\partial u_i}{\partial x_j}\right)=-\frac{\partial p}{\partial x_i}+\frac{\partial(2\mu(\phi)S_{ij})}{\partial x_j}-\rho(\phi)g\delta_{i3}+\gamma\kappa\delta_s(\phi)n_i. \tag{2.2}$$

Here, t is the time; ρ and μ are respectively the density and dynamic viscosity of the fluid; ϕ is the LS function, defined as the signed distance from the air–water interface with its value being positive and negative in water and air, respectively; p is the pressure; $S_{ij}=(\partial u_i/\partial x_j+\partial u_j/\partial x_i)/2$ is the strain rate tensor; g is the gravitational acceleration; δ_{ij} is the Kronecker delta tensor; γ is the surface tension; $\kappa=\nabla\cdot(\nabla\phi)$ at $\phi=0$ is the curvature of the air–water interface; $\delta_s(\phi)$ is the Dirac delta function at the interface; and $\boldsymbol{n}=[n_1, n_2, n_3]^{\mathrm{T}}=\nabla\phi$ at $\phi=0$ is the normal direction of the interface, orientating from water towards air. Periodic boundary conditions are imposed in x- and y-directions. No-slip boundary condition is applied at the bottom of water. At the top of air, the wind is driven by a constant shear stress τ_{top} in the streamwise direction, while shear-free ($\partial v/\partial z=0$) and impenetrable ($w=0$) conditions are prescribed for velocity components in y- and z-directions, respectively.

The computational domain size is set to $L_x\times L_y\times L_z=2\lambda\times 1.5\lambda\times 2.5\lambda$, where λ is the wavelength of the primary wave studied (figure 1). The mean elevation of water is set to $z=0$. The mean water depth d and air height h are 0.5λ and 2λ, respectively. The dispersion parameter kd is π, satisfying the deep water wave condition (Mei 1983), where $k=2\pi/\lambda$ is the wavenumber. The number of grid points used in the simulations is $N_x\times N_y\times N_z=320\times 192\times 360$. In the x- and y-directions, the grid is evenly spaced. In the z-direction, the grid is clustered between $z=-0.1\lambda$ and $z=0.15\lambda$ with a fine and constant resolution of $\Delta_z=0.002\lambda$, and the grid is stretched to the top of air and bottom of water. There are 286 and 74 grid points used for $z>0$ and $z<0$, respectively.

Equation (2.2) is spatially discretized using the second-order central difference scheme. The second-order Runge–Kutta (RK2) method is utilized for the time integration. At each sub-step of the RK2 method, the fractional-step method (Kim & Moin 1985) is used to enforce the divergence-free condition (2.1). The pressure is governed by the following Poisson equation (Yang *et al.* 2017)

$$\frac{\partial}{\partial x_i}\left(\frac{1}{\rho}\frac{\partial p}{\partial x_i}\right)=\frac{1}{\alpha\Delta t}\frac{\partial u_i^t}{\partial x_i}, \tag{2.3}$$

where α is a coefficient corresponding to the RK2 method, of which the value is 1.0 and 0.5 in the first and second sub-steps, respectively, Δt is the time step and u_i^t is the temporal velocity without considering the effect of the pressure term in (2.2). Equation (2.3) is solved using the Portable, Extensible Toolkit for Scientific Computation (PETSc) math library (Balay *et al.* 1997).

The air–water interfaces are tracked using the CLSVOF method. The LS method solves the following advection equation of the LS function

$$\frac{\partial\phi}{\partial t}+u_j\frac{\partial\phi}{\partial x_j}=0. \tag{2.4}$$

This equation is spatially discretized using the second-order essential non-oscillatory scheme (Shu & Osher 1989), and the second-order operator-splitting method (Sussman & Puckett 2000) is applied for the time integration. The reinitialization procedure of Sussman *et al.* (1994) is applied after solving (2.4) at every time step, such that ϕ maintains the property of a distance function $|\nabla\phi|=1$.

https://doi.org/10.1017/jfm.2018.466 Published online by Cambridge University Press

The LS function is coupled to the momentum (2.2) through the density and viscosity as

$$\rho = H(\phi, \Delta_s)\rho_w + [1 - H(\phi, \Delta_s)]\rho_a, \tag{2.5}$$

$$\mu = H(\phi, \Delta_s)\mu_w + [1 - H(\phi, \Delta_s)]\mu_a, \tag{2.6}$$

where the subscripts 'a' and 'w' represent air and water, respectively. The smoothed Heaviside function $H(\phi, \Delta_s)$ reads

$$H(\phi, \Delta_s) = \begin{cases} 0 & \phi < -\Delta_s, \\ \dfrac{1}{2}\left[1 + \dfrac{\phi}{\Delta_s} + \dfrac{1}{\pi}\sin\left(\dfrac{\phi\pi}{\Delta_s}\right)\right] & |\phi| \leqslant \Delta_s, \\ 1 & \phi > \Delta_s. \end{cases} \tag{2.7}$$

Here, Δ_s is set to three times the vertical grid size.

The mass conservation for each phase of fluid is enforced using the VOF method, which solves the following convection equation of the VOF function

$$\frac{\partial \psi}{\partial t} + \frac{\partial (u_j \psi)}{\partial x_j} = 0. \tag{2.8}$$

Here, ψ is defined as the volume fraction of water in a computational cell, from which it is known that $\psi = 0$ in the air, $\psi = 1$ in the water and $0 < \psi < 1$ in cells containing the air–water interface. The conservative VOF method (Weymouth & Yue 2010) is implemented to solve (2.8). The CLSVOF method of Sussman & Puckett (2000) is employed to couple ϕ and ψ, wherein the flux of ψ is calculated based on the interface reconstructed using the piecewise linear interface calculation (PLIC) algorithm with the help of ϕ, and the value of ϕ near the interface is determined using ψ. More detailed descriptions of the numerical method and validations are given in Liu (2012) and Yang *et al.* (2017).

3. Simulation cases

3.1. *Initialization of flow field*

The initial condition in the simulations is fully developed wind turbulence over strongly forced steep waves. Following the practice of many previous two-fluid numerical simulations of wave breaking (Chen *et al.* 1999; Iafrati 2009; Tian *et al.* 2010; Hu *et al.* 2012; Deike *et al.* 2015; Lubin & Glockner 2015; Deike *et al.* 2016), the initial water elevation is given as the analytical solution of Stokes wave at the third-order perturbation expansion of the wave steepness (Lamb 1932), *viz.*

$$\eta(x) = a_0 \cos(kx - \omega t) + \tfrac{1}{2}\varepsilon_0 a_0 \cos[2(kx - \omega t)] + \tfrac{3}{8}\varepsilon_0^2 a_0 \cos[3(kx - \omega t)], \tag{3.1}$$

where η is the surface elevation; a_0 is the initial amplitude of the linear wave component (the first term on the right-hand side of (3.1)); $\varepsilon_0 = ka_0$ is the initial linear wave steepness; and $\omega = \sqrt{gk(1 + \varepsilon_0^2)}$ is the angular frequency. The velocity in water is given correspondingly based on the potential flow theory (Lamb 1932). Equation (3.1) is used to prescribe the wave geometry, while the airflow is simulated based on the prescribed top shear stress and wave surface kinematics. Once the wind turbulence field is fully developed, the two-fluid flow field is output at different time as the initial condition for the different runs of the simulation of wind over breaking waves, such that the initial turbulence fluctuations vary among different runs. The air and water evolve dynamically from then on.

https://doi.org/10.1017/jfm.2018.466 Published online by Cambridge University Press

Group	Case	ε_0	c/u_*	Re_r	Re_s
	A55	0.55	3.7	2.51×10^6	180
I	B55	0.55	12.0	7.73×10^5	180
	C55	0.55	27.7	3.35×10^5	180
	A35	0.35	3.7	2.16×10^6	180
II	B35	0.35	12.0	6.66×10^6	180
	C35	0.35	27.7	2.89×10^6	180

TABLE 1. Specified computational parameters for airflow over breaking waves.

3.2. *Computational parameters*

Table 1 summarizes the key parameters of the simulation cases. Six cases have been considered, which can be categorized into two groups. Group I consists of cases A55, B55 and C55, in which $\varepsilon_0 = 0.55$ and plunging breakers are generated. We remark that the use of a very steep wave is a computationally effective method of initializing plunging breakers in numerical simulation (e.g. Chen *et al.* 1999; Iafrati 2009; Deike *et al.* 2015; Lubin & Glockner 2015; Yang *et al.* 2017). Generating plungers with the wave-focusing method (Derakhti & Kirby 2016) is more physical, but computationally more expensive especially with the incorporation of wind turbulence simulation. In future studies, with the increase of computer power, such approaches should be considered. The wave age c/u_* in cases A55, B55 and C55 is 3.7 (young wave), 12.0 (intermediate wave) and 27.7 (old wave), respectively (Sullivan *et al.* 2000; Yang & Shen 2010). Here, $c = \omega/k$ characterizes the phase speed of the initial prescribed wave, and $u_* = \sqrt{\tau_{top}/\rho_a}$ is the frictional velocity in the air. Group II consists of cases A35, B35 and C35, in which $\varepsilon_0 = 0.35$ and spilling breakers are generated. The waves ages in the group II cases are the same as those in the group I cases. If we consider waves with $\lambda = 20$ m, the Reynolds number $Re_r = u_*\lambda/\nu_a$ is $O(10^{5\sim6})$. We reduce the Reynolds number to $Re_s = 180$ in the present study to perform DNS. Although large-eddy simulation (LES) is a possible tool for simulating wind turbulence over breaking waves at high Reynolds numbers, there are many challenges associated with LES. For example, the subgrid-scale modelling for air–water mixed flow and the wall-layer modelling near the complex wave surface with flow separation need substantial further studies, which are however, beyond the scope of this paper. In this study, we chose to use DNS because it has the advantage that the flow processes are directly captured, and no *ad hoc* turbulence modelling is needed. The reduction of the Reynolds number thickens the boundary layer of wind attached to the wave surface. Nevertheless, based on their numerical simulation results, Deike *et al.* (2015) concluded that the Reynolds number does not play an important role in the breaking process. Instead, the wave steepness is the key parameter. Their conclusion was supported by previous laboratory experiments (Rapp & Melville 1990; Perlin *et al.* 1993; Zhang 1995; Fedorov *et al.* 1998; Duncan *et al.* 1999; Jiang *et al.* 1999; Tulin & Waseda 1999; Duncan 2001; Liu & Duncan 2003, 2006; Banner & Peirson 2007; Drazen *et al.* 2008; Caulliez 2013, see also table 1 in Deike *et al.* 2015).

3.3. *Definition of turbulent statistics*

Because the wave breaking of interest is highly unsteady and intermittent, time averaging cannot be used to define turbulent statistics in the present study of wind

https://doi.org/10.1017/jfm.2018.466 Published online by Cambridge University Press

over breaking waves. Alternatively, we conduct many ensemble runs for each case starting with the same mean flow but with different initial fluctuations (§ 3.1), so that the ensemble over all runs can be used to calculate turbulence statistics. To be specific, in different runs of the same case, the initial wind profile and wave geometry are the same, but the instantaneous turbulence fluctuations are different. Once an initial field is obtained, the time of this field is set to $t=0$ for the simulation of wind over breaking waves. We run each sample till $t=3.0T$, after which the wave breaking becomes less violent (see figure 4). Here, $T=2\pi/\omega$ is the period of the third-order Stokes waves based on the potential flow theory.

According to the above descriptions, it is understood that each field variable f is a function of not only x, y, z and t, but also the sample index n_s. We define ensemble averaging as

$$\bar{f}(x_i, z_k, t)=\frac{1}{N_w N_s N_y}\sum_{n_w=0}^{N_w-1}\sum_{n_s=1}^{N_s}\sum_{j=1}^{N_y} f(x_i+n_w\lambda, y_j, z_k, t, n_s), \tag{3.2}$$

where the overbar denotes an ensemble-averaged quantity. The subscripts i, j and k are the indices of discretized grid points in the x-, y- and z-directions, respectively; $N_w=2$ is the number of waves within the streamwise computational domain; $N_s=100$ is the total number of samples. The fluctuations with respect to the ensemble averaging are defined as

$$\left.\begin{array}{ll} f''(x, y, z, t, n_s)=f(x, y, z, t, n_s)-\bar{f}(x, z, t) & \text{for } 0\leqslant x\leqslant\lambda, \\ f''(x, y, z, t, n_s)=f(x, y, z, t, n_s)-\bar{f}(x-\lambda, z, t) & \text{for } \lambda\leqslant x\leqslant 2\lambda. \end{array}\right\} \tag{3.3}$$

Note that f and $\bar{f}$ are defined in $[0, 2\lambda]$ and $[0, \lambda]$ in the x-direction, respectively. As a result, the definition of f'' is given separately in $[0, \lambda]$ and $[\lambda, 2\lambda]$ in (3.3).

An ensemble-averaged quantity $\bar{f}$ can be further decomposed into a plane-averaged part $\langle f\rangle$ and a wave-coherent part $\tilde{f}$ as

$$\bar{f}(x, z, t)=\langle f\rangle(z, t)+\tilde{f}(x, z, t), \tag{3.4}$$

where the plane averaging is defined as

$$\langle f\rangle(z, t)=\frac{N_w}{N_x}\sum_{i=1}^{N_x/N_w}\bar{f}(x_i, z, t). \tag{3.5}$$

The fluctuation $f'(x, y, z, t, n_s)$ with respect to the plane averaging is defined as

$$f'(x, y, z, t, n_s)=f(x, y, z, t, n_s)-\langle f\rangle(z, t). \tag{3.6}$$

By substituting (3.4) into (3.3), a triple decomposition is obtained as

$$f=\langle f\rangle+\tilde{f}+f''. \tag{3.7}$$

Triple decomposition has been used to analyse the airflow over non-breaking waves (e.g. Hsu, Hsu & Street 1981; Sullivan *et al.* 2000; Yang & Shen 2010; Druzhinin *et al.* 2012). According to (3.6) and (3.7), the fluctuation with respect to

https://doi.org/10.1017/jfm.2018.466 Published online by Cambridge University Press

the plane averaging f' can be decomposed into the fluctuation with respect to the ensemble-averaged part f'' and the wave-coherent part $\tilde{f}$ as

$$f' = \tilde{f} + f''. \tag{3.8}$$

It can be proven from (3.2) that the ensemble averaging of the wave-coherent fluctuation is trivial, i.e.

$$\bar{\tilde{f}} = 0. \tag{3.9}$$

Based on (3.8) and (3.9), it can be further derived that the total momentum flux $\overline{u_i' u_j'}$ can be decomposed into the contributions from u_i'' and $\tilde{u}_i$ as

$$\overline{u_i' u_j'} = \overline{u_i'' u_j''} + \overline{\tilde{u}_i \tilde{u}_j}. \tag{3.10}$$

By applying (3.5), it is known that a similar decomposition holds for the total momentum flux with respect to the plane averaging as

$$\langle u_i' u_j' \rangle = \langle u_i'' u_j'' \rangle + \langle \tilde{u}_i \tilde{u}_j \rangle. \tag{3.11}$$

We note here that we have tested the effects of N_w and N_s on the simulation results of turbulence statistics. We have run case A55 using a larger computational domain with $L_x = 4\lambda$ and $N_w = 4$. We found that the results demonstrated in this paper are not altered. We have also performed a sample-number convergence test for case A55. The results obtain from $N_s = 50$, 100 and 200 are compared with each other. We found that increasing the number of samples results in a negligibly small change of turbulence statistics. For example, the plane-averaged streamwise velocity $\langle u \rangle$ for the three N_s varies less than 1 %. The difference in the total momentum flux $\langle u'w' \rangle$ is less than 4 % between $N_s = 50$ and 100, and is less than 2 % between $N_s = 100$ and 200.

4. Results

4.1. *Validation*

Figure 2(*a*) shows the surfaces of breaking waves with $\epsilon = 0.35$ without wind, from $t = 0$ to $3.0T$. The wave surface at t is shifted by ct/λ in the $+z$-direction. The time interval between two wave surfaces is $0.1T$. As shown, the breaking is gentle, and the wave amplitude decreases slowly. This observation is consistent with the results of Iafrati (2009). Figure 2(*b*) further compares the total energy E/E_0 with the results of Iafrati (2009) and Deike *et al.* (2015). Here, E is the mechanical energy, defined as the summation of the potential energy E_p and the kinetic energy E_k of water, and E_0 is the value of E at $t = 0$. The definitions of E_p and E_k are given respectively as

$$E_p = \int \rho(z + d/2)\, \mathrm{d}V, \tag{4.1}$$

and

$$E_k = \frac{1}{2} \int \rho(u^2 + v^2 + w^2)\, \mathrm{d}V. \tag{4.2}$$

In (4.1), d is the water depth (see § 2). The integrations in (4.1) and (4.2) are performed in the water. Figure 2(*b*) shows that the present results agree with those in the literature. The test results on the accuracy of our code in simulating non-breaking and breaking waves are also given in Hu *et al.* (2012) and Liu (2012).

https://doi.org/10.1017/jfm.2018.466 Published online by Cambridge University Press

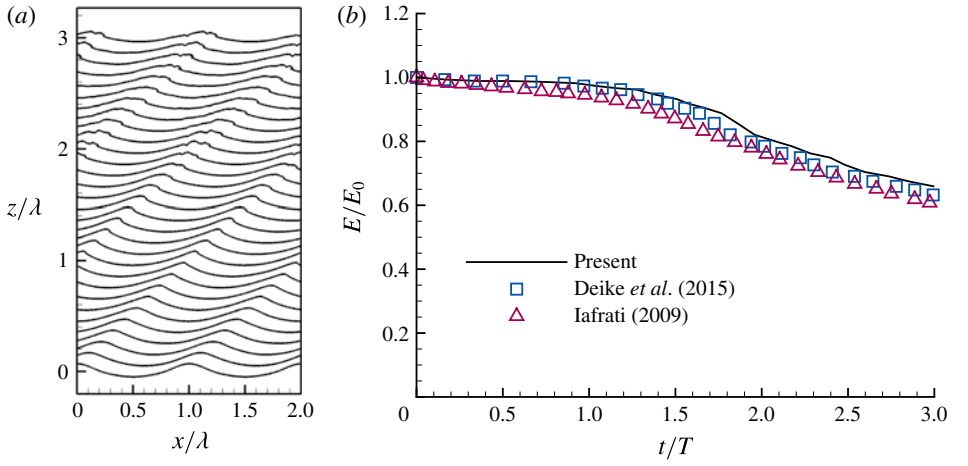


FIGURE 2. (Colour online) Simulation results for wave breaking with $\epsilon = 0.35$ and $u_* = 0$. (*a*) Wave geometry from $t = 0$ to $3.0T$. The wave surface is shifted by ct/λ in the $+z$-direction. (*b*) Time series of total energy E.

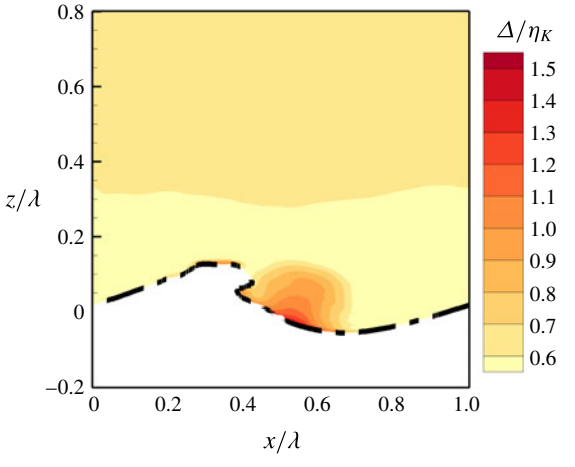


FIGURE 3. (Colour online) Contours of the ratio between the grid resolution Δ and Kolmogorov length scale η_K at $t = 0.8T$ in case A55. The thick dash-dotted line represents the upper bound of wave surfaces.

4.2. *Resolution study*

We have examined the grid resolution to confirm that it is sufficient for performing DNS of wind over breaking waves. Figure 3 displays the contours of the ratio between the grid size $\Delta = (\Delta_x\Delta_y\Delta_z)^{1/3}$ and Kolmogorov length scale $\eta_K = (\nu_a^3/\epsilon)^{1/4}$ at $t = 0.8T$ in case A55. Here, $\epsilon = \nu\overline{a''_{ij}a''_{ij}}$ is the dissipation rate of turbulence kinetic energy (TKE), with $a''_{ij} = \partial u''_i/\partial x_j$ being the fluctuation of the velocity gradient tensor. It is demonstrated in figure 3 that the value of Δ/η_K is smaller than 1.4 in the bulk of air. We have also examined the grid resolution at different instants (from $t = 0$ to $t = 3.0T$ with an interval of $0.1T$) in all simulation cases listed in table 1. The maximum of Δ/η_K is smaller than 1.6, indicating that the grid resolution of the DNS is satisfied

https://doi.org/10.1017/jfm.2018.466 Published online by Cambridge University Press

in the present study (Eswaran & Pope 1988). Because we focus on the airflow in the present study, we show only the resolution in the air phase. In fact, the grid resolution normalized by the Kolmogorov scale is more adequate in water than in air due to the lower Reynolds number in water.

We note here that the instantaneous wave surface varies with the spanwise coordinate y. Moreover, it differs among different ensemble runs. Therefore, the air–water interfaces should not be represented deterministically by a single line in a 2-D plot of ensemble-averaged statistics. In this paper, we use a thick dash-dotted line to denote the upper bound of all interfaces (figure 3). There are different approaches for defining the upper bound. The most strict definition corresponds to $\bar{\psi} = 0$, above which no water is found in any spanwise plane and in any sample. However, as pointed out by Brocchini & Peregrine (2001), because some small water droplets can be convected far away from the wave surface, it is more practical to use $\bar{\psi} = 0.05$ to define the upper bound, which is adopted in the present study. In the region between the upper and lower bounds of the interfaces, the mean density is the fractional-averaged value of the densities of air and water, which varies spatially. In this sense, the flow is statistically compressible in this region (Hong & Walker 2000; Chassaing *et al.* 2002; Hendrickson *et al.* 2013). Because we focus on the airflow in the present study, we only consider the flow field above the upper bound to reduce the complexity of the transport equations of the mean velocity and TKE.

4.3. *Instantaneous wave surface*

The process of wave breaking has been described in many papers (e.g. Duncan 1981, 1983; Longuet-Higgins 1982; Bonmarin 1989; Chen *et al.* 1999; Tulin & Waseda 1999; Iafrati 2009; Deike *et al.* 2015). The geometries of plunging and spilling breakers obtained from the present simulations are consistent with those observed in previous numerical simulations (Chen *et al.* 1999; Iafrati 2009; Deike *et al.* 2015; Lubin & Glockner 2015). We demonstrate representative 3-D wave surfaces at different stages of wave breaking in this section. The plunging and spilling breakers are described based on cases A55 and A35, respectively.

Figure 4 shows successive snapshots of instantaneous wave surfaces visualized using the isosurface of $\phi = 0$ in case A55. The initial geometry of the wave surface is plotted in figure 4(*a*). The wave front is steepened and becomes almost vertical at $t = 0.3T$ (figure 4*b*). An overturning jet is then formed at the wave front at $t = 0.8T$ (figure 4*c*). The jet impinges onto the wave surface, causing splash-up events at $t = 1.0T$ (figure 4*d*). At $t = 3.0T$ (figure 4*e*), the waves keep breaking but the wave steepness is much smaller than that before the wave breaking (figure 4*a*).

Figure 5 shows the characteristic snapshots of spilling breaking waves in case A35. Different from case A55, no overturning jet is generated in case A35. Instead, as displayed in figure 5(*b*), a bulge is formed when the wave front is steepened. Figure 5(*c*,*d*) shows that the bulge grows during wave breaking, and the wave surface is roughened behind (to the left in the figure) the wave crest.

4.4. *Mean velocity*

Figure 6(*a*) compares the vertical profiles of the plane-averaged mean streamwise velocity $\langle u \rangle$ normalized by u_* at different time instants in case A35. Figure 6(*b–d*) shows respectively the vertical profiles of $\langle u \rangle / u_*$ in cases A55, B55 and C55, with the results in the respective cases A35, B35 and C35 at $t = 0.0T$ superposed for comparison. Because the plane averaging is undefined below the wave crest, the

https://doi.org/10.1017/jfm.2018.466 Published online by Cambridge University Press

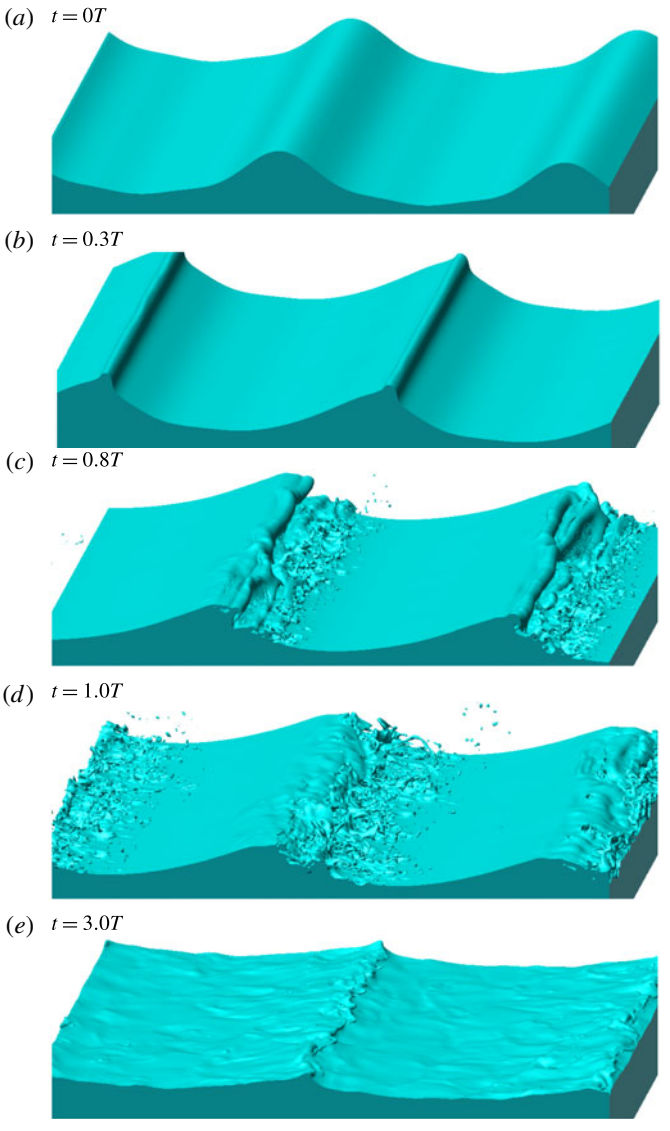


FIGURE 4. (Colour online) Successive snapshots of instantaneous wave surface of plunging breakers in case A55. The waves propagate from left to right.

lowest point of the profile is away from $z = 0$, which is different from the analyses of turbulence statistics on wave-surface-fitted grid (Hara & Sullivan 2015). As shown in figure 6(*a*), the profile of $\langle u \rangle$ changes little during the spilling breaking process in case A35. Similarly, spilling breakers do not alter the profiles of $\langle u \rangle$ much in cases B35 and C35, so that we only show results at $t = 0.0T$ in these two cases to keep the paper concise.

Figure 6(*b*) shows that at $t = 0.0T$, the magnitude of $\langle u \rangle$ below $z/\lambda = 0.4$ is slightly larger in case A35 than in case A55, but it is less sensitive to the wave steepness above $z/\lambda = 0.4$. In the intermediate and old wave cases, $\langle u \rangle$ is more sensitive to the wave steepness. As demonstrated in figure 6(*c*), at $t = 0.0T$, $\langle u \rangle$ below $z/\lambda = 0.8$ is

https://doi.org/10.1017/jfm.2018.466 Published online by Cambridge University Press

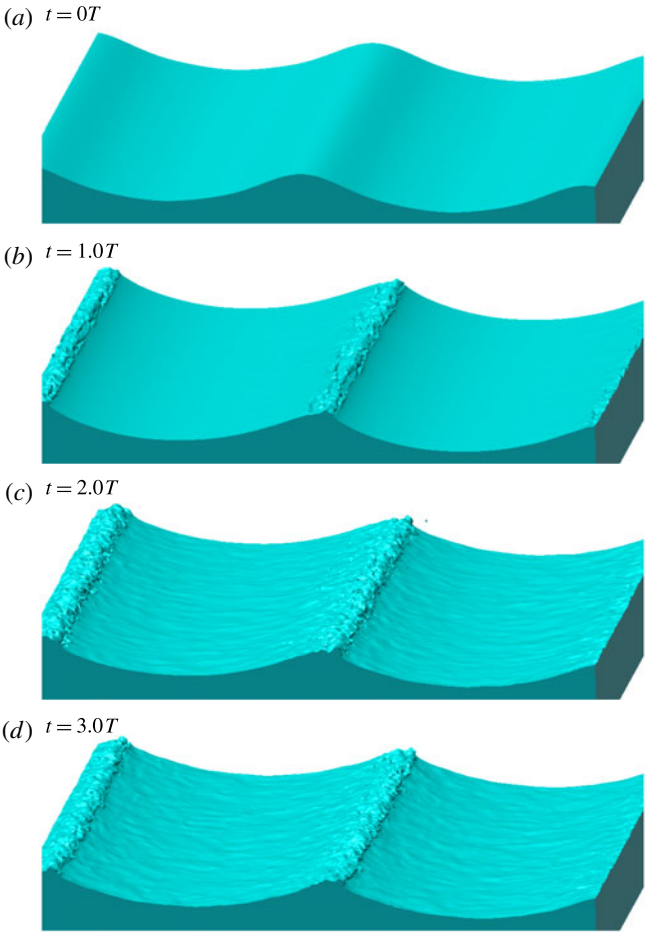


FIGURE 5. (Colour online) Successive snapshots of instantaneous wave surface of spilling breakers in case A35. The waves propagate from left to right.

larger in case B35 than in case B55. Figure 6(*d*) shows that the profiles of $\langle u \rangle$ in cases C35 and C55 are drastically different. The vertical gradient of $\langle u \rangle$ is positive in case C35, but it is negative below $z/\lambda = 0.3$ in case C55. The negative velocity gradient near the wave surface is consistent with previous simulation results of wind over non-breaking waves at large wave age (Jiang *et al.* 2016). A further discussion on the negative velocity gradient in case C55 is given in § 4.5.

Near the wave surface, the profiles of $\langle u \rangle$ in group I cases are sensitive to the violent plunging wave breaking. As demonstrated in figure 6(*b–d*), the magnitude of $\langle u \rangle$ near the wave surface is larger at $t = 3.0T$ than at $t = 0.0T$ in all of the three group I cases, indicating the overall transport of momentum from water to air during the wave plunging at various wave ages. However, it is observed in figure 6(*b*) that in case A55, $\langle u \rangle$ experiences a transient decrease above $z/\lambda = 0.2$ before $t = 1.0T$. Figure 6(*c*,*d*) shows respectively that in cases B55 and C55, the magnitude of $\langle u \rangle$ decreases slightly below $z/\lambda = 0.2$ after $t = 2.0T$. A further analysis on the response of $\langle u \rangle$ to the wave plunging is given in § 4.5 together with the total momentum flux $\langle u'w' \rangle$.

https://doi.org/10.1017/jfm.2018.466 Published online by Cambridge University Press

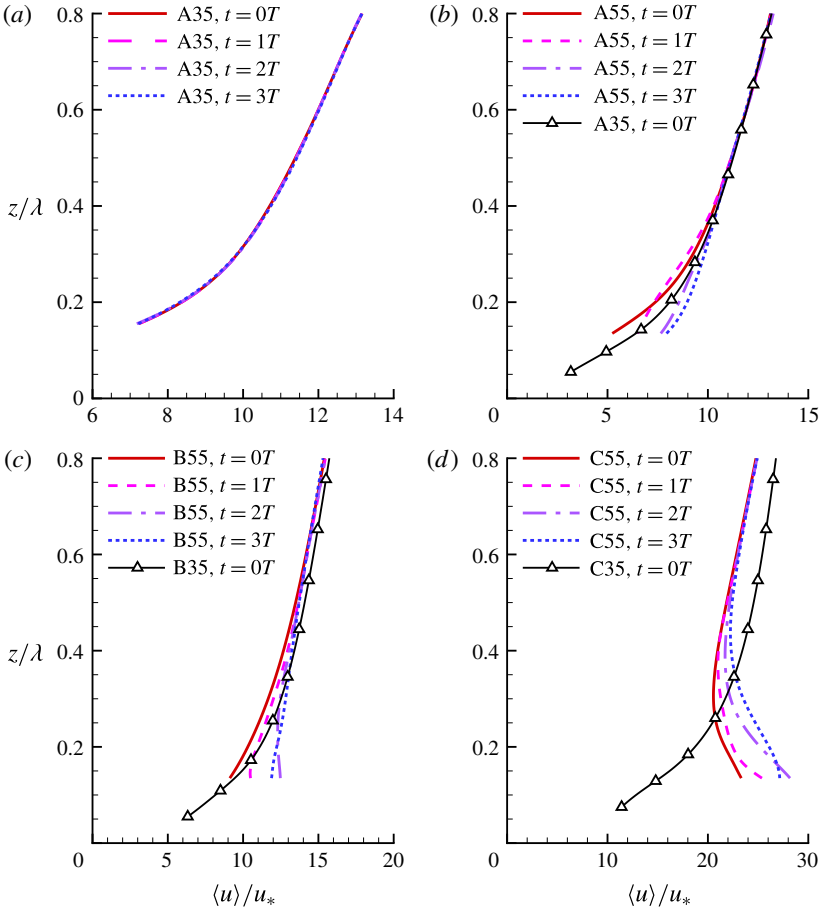


FIGURE 6. (Colour online) Vertical profiles of plane-averaged mean streamwise velocity $\langle u\rangle/u_*$ in cases (*a*) A35, (*b*) A55, (*c*) B55 and (*d*) C55. The results of cases A35, B35 and C35 at $t = 0.0T$ are plotted respectively in (*b–d*) for comparison.

Figure 7 shows the ensemble-averaged mean streamwise velocity $\bar{u}$, mean vertical velocity $\bar{w}$, and mean spanwise vorticity $\bar{\omega}_y$ near the wave surface at successive time instants in case A55. Note that the flow physics far away from the wave surface are dominated by wind, so that we use the characteristic velocity scale of wind u_* to non-dimensionalize $\langle u\rangle$ in figure 6. In contrast, the effects of waves are dominant near the wave surface, and as a result, we use c as the characteristic velocity scale in figure 7. As introduced in § 4.2, the thick dash-dotted line represents the upper bound of wave surfaces in different spanwise planes and simulation samples, which is different from instantaneous wave surface. For comparison, we also plot an instantaneous air–water interface at an x–z plane using the dotted line in figure 7. At $t = 0.0T$, the instantaneous wave surface collapses to the upper bound of interfaces, such that only the upper bound is shown in figure 7(*a*). It can be observed from figure 7(*b–e*) that at later times, the dotted lines are below the dash-dotted lines, which is expected based on the definition of the upper bound of interfaces given in § 4.2. Also note that as explained in § 3, ensemble-averaged quantities are defined in the region $[0, \lambda]$ in the streamwise direction. Due to the use of the periodic boundary

https://doi.org/10.1017/jfm.2018.466 Published online by Cambridge University Press

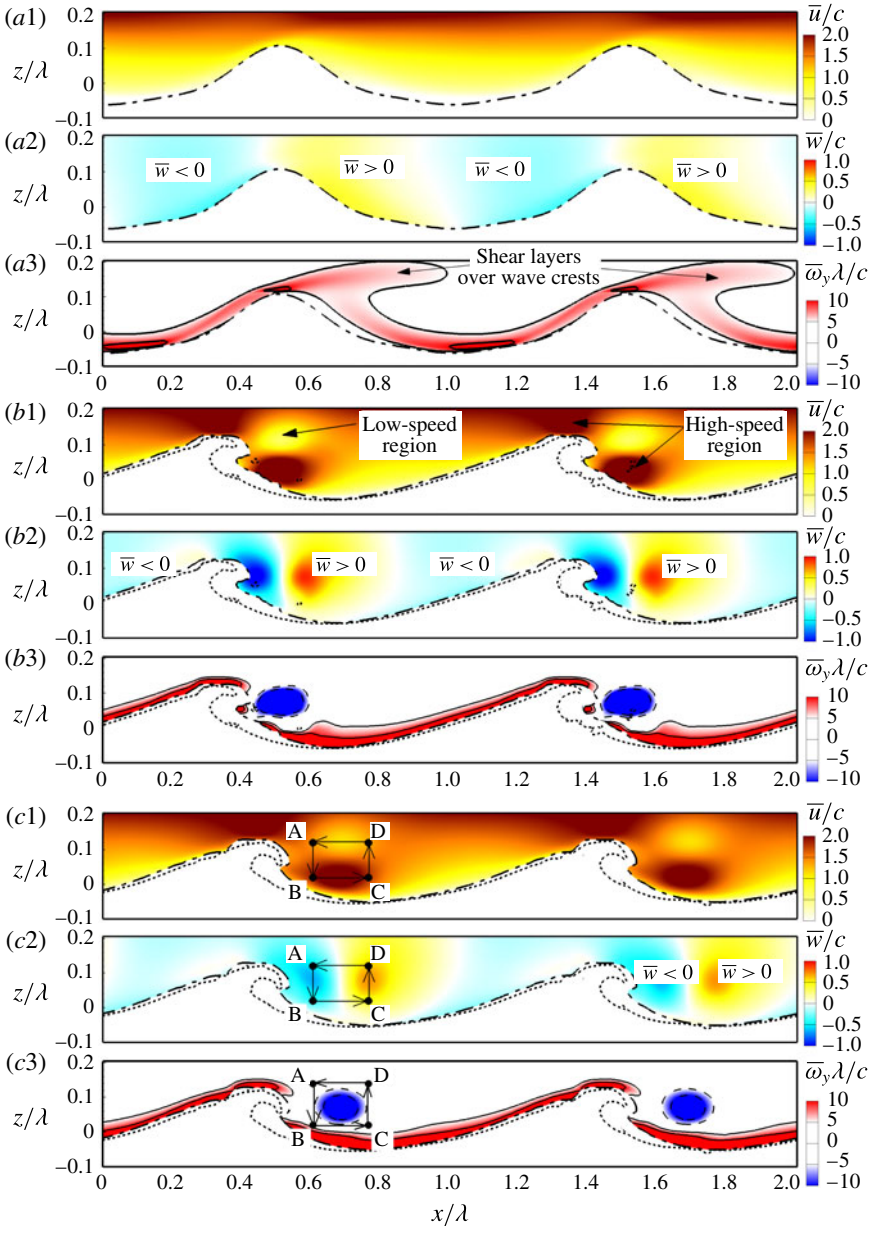


FIGURE 7. For caption see next page.

condition in the streamwise direction, we show the results in the region $[0, 2\lambda]$ by duplicating the flow field in $[0, \lambda]$ to $[\lambda, 2\lambda]$. This ensures that all flow structures can be demonstrated in a continuous frame.

As demonstrated in figure 7(*a*2), when the wave is onset to break, the vertical velocity is negative and positive on the windward and leeward of the wave crest, respectively. This can be explained by the fact that the vertical component of the orbital velocity at the wave surface is positive on the leeward, and is negative on the

https://doi.org/10.1017/jfm.2018.466 Published online by Cambridge University Press

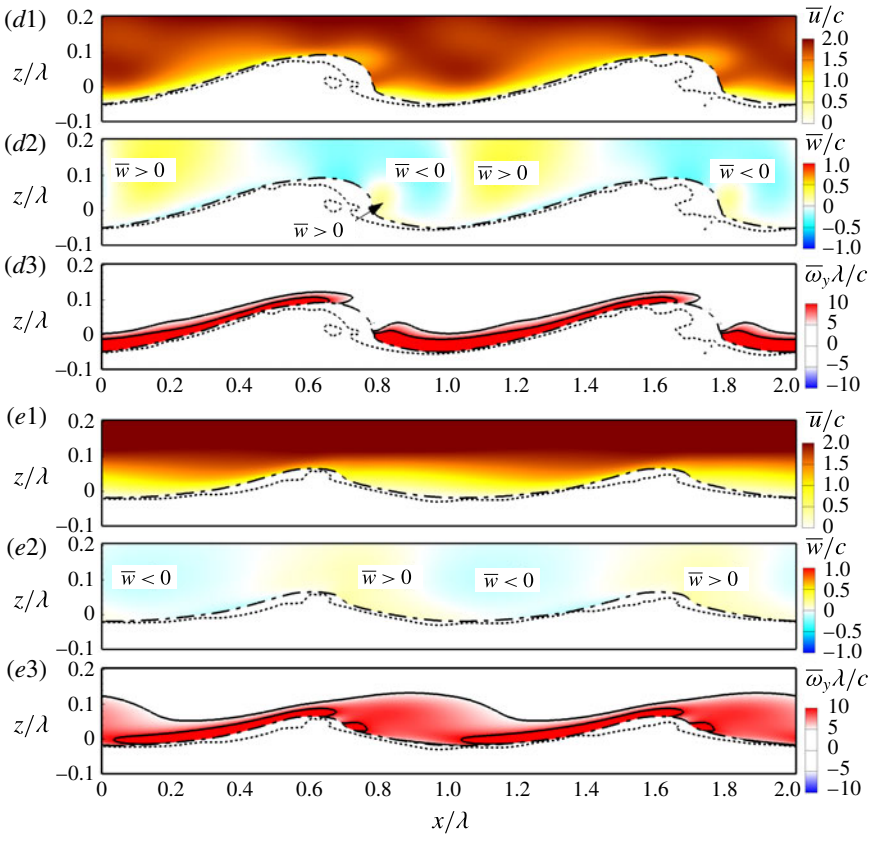


FIGURE 7 (cntd). (Colour online) Phase-averaged flow field at (*a*) $t = 0.0T$, (*b*) $t = 0.7T$, (*c*) $t = 0.8T$, (*d*) $t = 1.0T$ and (*e*) $t = 3.0T$ in case A55. Mean streamwise velocity $\bar{u}$, mean vertical velocity $\bar{w}$, and mean spanwise vorticity ω_y are shown in panels 1, 2 and 3, respectively. The dotted line demonstrates an instantaneous air–water interface in a spanwise plane. The dash-dotted line represents the upper bound of all wave surfaces (see § 4.2 for the definition). The solid and dashed lines in panel 3 represent positive and negative isopleths of $\omega_y\lambda/c$, respectively. The interval of the isopleths is 5. The wave propagates in the $+x$-direction.

windward. Therefore, the wave pushes the air on the leeward to move upward, while the air on the windward moves downward to follow the motion of the wave surface.

Figure 7(*a*3) shows that at $t = 0.0T$, the vorticity near the leeward of the wave surface is of small magnitude, and a shear layer detached from the wave surface appears in the downstream of the wave crest. This indicates that air particles do not move downward along the wave surface when they flow past the wave crest. Instead, they move upward, and a separation region is developed on the leeward of the wave surface. The airflow separation is consistent with observations from laboratory experiments (Banner & Melville 1976; Reul *et al.* 1999; Veron *et al.* 2007; Reul *et al.* 2008; Buckley & Veron 2016).

The overturning jet (figure 7*b*,*c*) formed during the first plunging event alters the flow structures significantly. When the jet impinges onto the wave surface,

https://doi.org/10.1017/jfm.2018.466 Published online by Cambridge University Press

it pushes the air to move forward. This process accelerates the airflow in the streamwise direction, and as a result, a high-speed region is developed ahead of the wave front (figure 7*b*1,*c*1). Meanwhile, the jet brings the air particles around it to impinge onto the wave surface. Therefore, the vertical velocity of airflow displayed in figure 7(*b*2,*c*2) becomes negative on the leeward of the wave crest, and the airflow separation over the wave crest is weakened. This is evident from figure 7(*b*3,*c*3), which shows that the detached shear layer downstream of the wave crest is significantly weakened. Furthermore, figure 7(*b*2) shows that the upward-moving air on the leeward is pushed away from the wave surface, and a counterclockwise-rotating vortex is generated between the downward and upward airflow. This vortex corresponds to the negative vorticity in figure 7(*b*3,*c*3). The airflow above the vortex is decelerated to compensate the air moving downward with the jet, such that a low-speed region appears above the vortex (figure 7*b*1,*c*1).

From the comparison between figure 7(*a*1,*e*1), it can be seen that the streamwise velocity above the wave crest increases during the wave breaking in case A55. This observation is consistent with the plane-averaged mean velocity $\langle u \rangle$ shown in figure 6(*b*). Two physical processes responsible for the acceleration of wind can be observed from figure 7. The first process corresponds to the air motion around the large-scale vortex. As illustrated in figure 7(*c*), when the airflow goes along the cycling routine ABCDA, the low-speed air moves downward with the jet from A to B, and is then accelerated from B to C. The high-speed air moves upward from C to D, losing momentum to the flow above the wave crest. Finally, the low-speed air moves back to point A (note that the mean streamwise velocity is positive in the earth frame plotted, but is negative in the frame travelling with the wave) and starts a new cycle. In this process, the vortex transports the high-speed air from the region ahead of the wave front to that above the wave crest. The second process lies in the fact that the velocity of water near the wave crest increases during wave breaking. Correspondingly, the air velocity above the wave crest is also accelerated. This is evident from figure 7(*b*1,*c*1), which shows that a high-speed region occurs over the wave crest. The two mechanisms are both associated with the first plunging event. As a result, the plane-averaged velocity near the wave crest increases more significantly before $t = 1.0T$ than after that. For example, figure 6(*b*) shows that the value of $\langle u \rangle / u_*$ at $z/\lambda = 0.1$ increases by 48 % before $t = 1.0T$, whereas it increases by only 12 % after that.

Figure 8 shows the ensemble-averaged mean streamwise velocity $\bar{u}$, mean vertical velocity $\bar{w}$ and mean spanwise vorticity $\bar{\omega}_y$ in case B55 for the wave with intermediate wave age (table 1). Figure 8(*a*1) does not show a shear layer over the wave crest in case B55 before the wave breaking, indicating that airflow separation is not evident at larger wave age. This is consistent with the observation in the laboratory experiment of Buckley & Veron (2016). Similar to case A55, a spanwise vortex with negative $\bar{\omega}_y$ is generated during the first plunging event (figure 8*b*3). From the comparison between figure 8(*a*1,*c*1), it is known that the mean velocity at the late stage of wave breaking ($t = 3.0T$) is slightly larger than that before wave breaking ($t = 0.0T$). Such an acceleration effect of wave breaking on the mean streamwise velocity is similar to that at small wave age in case A55.

Figure 9 shows the ensemble-averaged flow field in case C55 with large wave age (table 1). Similar to case B55 (figure 8*a*3), airflow separation is not evident in case C55 (figure 9*a*3). As shown in figure 9(*b*3), the wave breaking also generates a

https://doi.org/10.1017/jfm.2018.466 Published online by Cambridge University Press

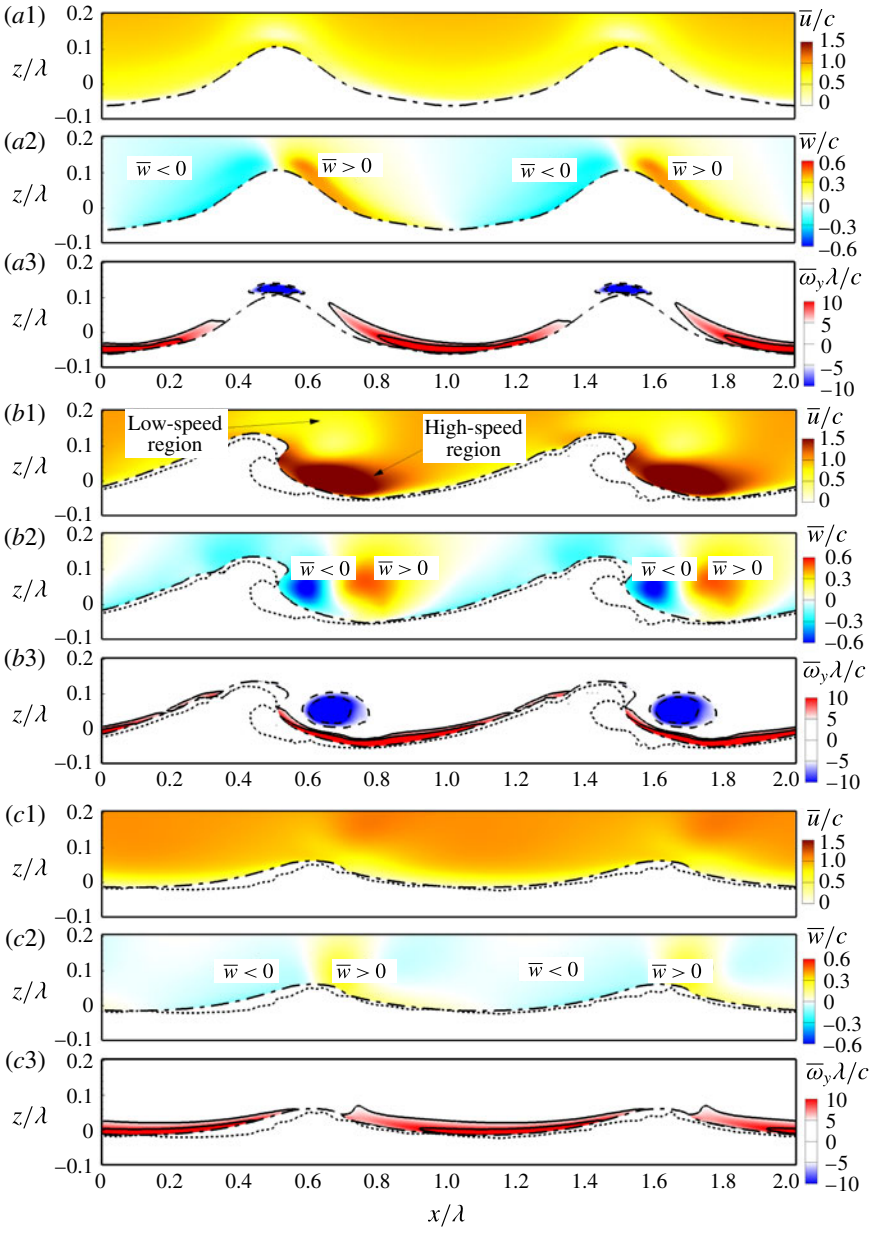


FIGURE 8. (Colour online) Phase-averaged flow field at (*a*) $t = 0.0T$, (*b*) $t = 0.8T$ and (*c*) $t = 3.0T$ in case B55. See figure 7 for the detailed caption.

spanwise vortex in case C55. From the comparison among figures 7(*c*1), 8(*b*1) and 9(*b*1), it can be seen that the streamwise scale of the high-speed region is larger in case C55 than in cases A55 and B55. The vortex also expands in the streamwise direction in case C55. It is known from the comparison between figure 9(*a*1,*c*1) that

https://doi.org/10.1017/jfm.2018.466 Published online by Cambridge University Press

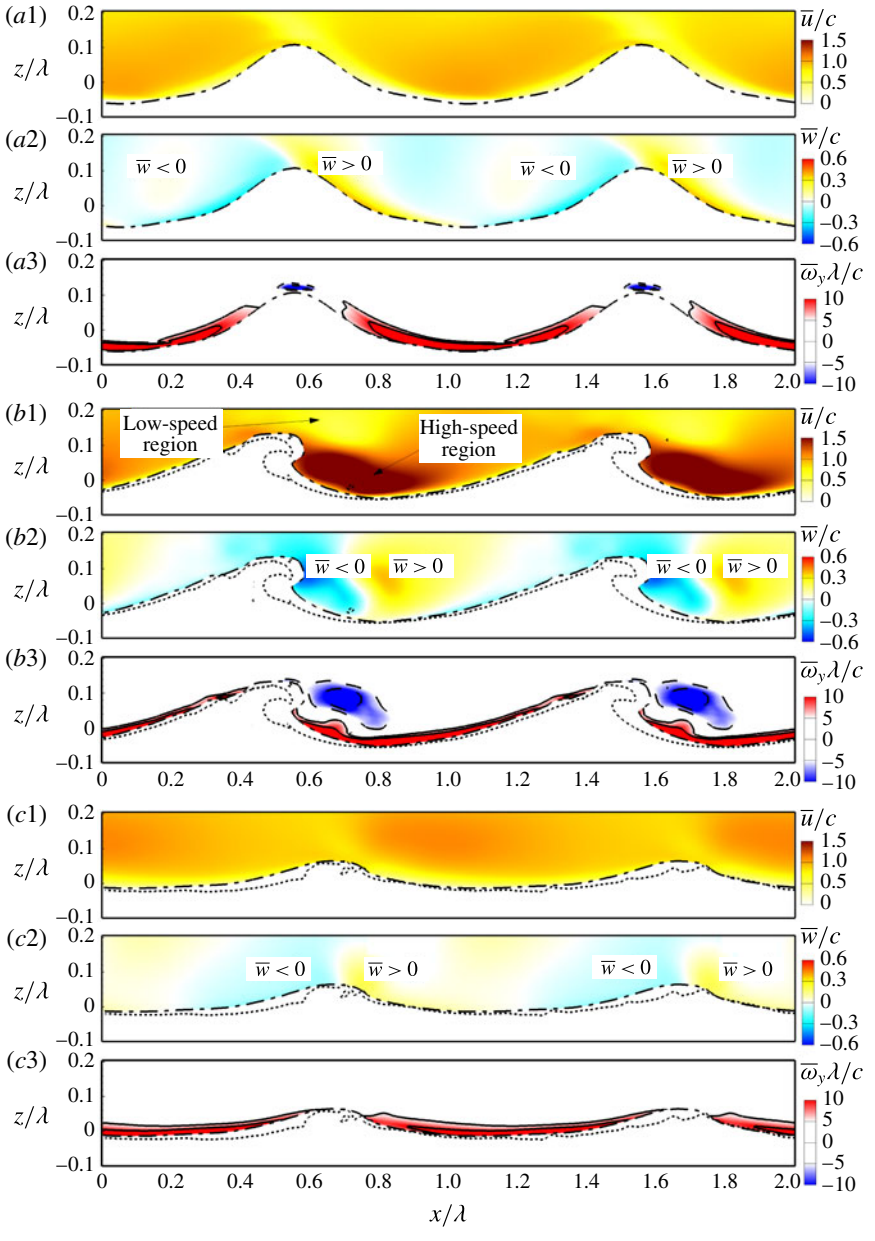


FIGURE 9. (Colour online) Phase-averaged flow field at (*a*) $t = 0.0T$, (*b*) $t = 0.8T$ and (*c*) $t = 3.0T$ in case C55. See figure 7 for the detailed caption.

a plunging beaker with large wave age also causes the increase of the air velocity. This is consistent with the observation from figures 7 and 8 for cases A55 and B55, respectively, and is also consistent with the result of the plane-averaged mean velocity $\langle u \rangle$ shown in figure 6(*d*).

https://doi.org/10.1017/jfm.2018.466 Published online by Cambridge University Press

To further study the effect of wave breaking on the mean velocity, we analyse the transport equation of the integral mean velocity, which reads

$$\frac{\partial}{\partial t}\int_{\Omega}\overline{u}\,\mathrm{d}V = \underbrace{-\int_{TB}\overline{uu_{ri}}n_i\,\mathrm{d}s}_{C_{TB}}\underbrace{-\int_{TB}\frac{\bar{p}}{\rho_a}n_1\,\mathrm{d}s}_{\Pi_{TB}}+\underbrace{\int_{TB}\nu_a\frac{\partial\bar{u}}{\partial x_i}n_i\,\mathrm{d}s}_{D_{TB}} + \underbrace{\lambda\langle uw\rangle|_{z_1}}_{C_1}+\underbrace{\lambda\nu_a\left.\frac{\partial\langle u\rangle}{\partial z}\right|_{z_1}}_{D_1}. \tag{4.3}$$

The equation above is derived by performing ensemble averaging on (2.2), and integrating the resultant equation in a control volume Ω between the top bound (denoted by TB in the equation) of the wave surfaces and the horizontal plane at $z_1 = 0.14\lambda$, which is chosen to ensure that the wave crest is close but below it. It is shown in the following analyses that the evolution of the mean streamwise velocity near the wave surface is dominated by the momentum fluxes across the wave surface. Changing the value of z_1 does not alter our conclusions. Note that according to the definition of the ensemble averaging (3.2), Ω is a 2-D geometry, while the top bound of wave surfaces and horizontal plane reduce to lines in (4.3). The left-hand side of (4.3) is the material derivative of the integral mean velocity. The first, second and third terms on the right-hand side of (4.3) are respectively the convection flux C_{TB}, pressure flux Π_{TB} and viscous flux D_{TB} across the top bound of wave surfaces, where $\boldsymbol{u}_r = [u_{r1}, u_{r2}, u_{r3}]$ is the relative velocity of airflow with respect to the moving speed of the top bound of wave surfaces, with $\boldsymbol{n} = [n_1, n_2, n_3]$ being its normal direction, pointing from air into water. Because the top bound of wave surfaces is not a material surface, fluid particles can cross it, resulting in a relative velocity between the airflow and top bound. However, this relative velocity is small, and as a result, the convection flux does not play a major role at the top bound of the wave surface, which is evident from the results shown below. The fourth and fifth terms on the right-hand side of (4.3) are respectively the convection flux C_1 and viscous flux D_1 across plane z_1. Note that the definition of the plane averaging (3.5) is used to derive the last two terms.

Figure 10 compares the time series of the flux terms on the right-hand side of equation (4.3) in cases A35, A55, B55 and C55. The total flux is also shown in the figure. All fluxes in figure 10 are normalized using λc^2. At $t = 0.0T$, the initial field is a fully developed turbulent flow, so that the total flux is negligibly small, i.e. the flux terms are balanced, in all cases. In cases A35 and A55 (figure 10*a*,*b*) for young waves, the pressure flux at the top bound of wave surface Π_{TB} is negative. In case B55 for the intermediate waves (figure 10*c*), the magnitude of Π_{TB} becomes significantly smaller. In case C55 (figure 10*d*) for the old waves, Π_{TB} reverses its sign to be positive. It has also been reported in the literature of wind over non-breaking waves (Sullivan *et al.* 2000; Yang & Shen 2010) that the value of pressure flux at the wave surface increases as the wave age increases.

Figure 10(*a*) shows that all fluxes change little during wave breaking in case A35 with spilling breakers. As a result, the mean streamwise velocity $\langle u\rangle$ shown in figure 6(*a*) does not change much. In contrast, with plunging breakers, the total flux increases rapidly before $t = 0.7T$ in cases A55, B55 and C55. The pressure flux is the dominant term that causes the increase of the total flux. As shown in figure 10(*b–d*), the pressure flux increases significantly after $t = 0.3T$. To further

https://doi.org/10.1017/jfm.2018.466 Published online by Cambridge University Press

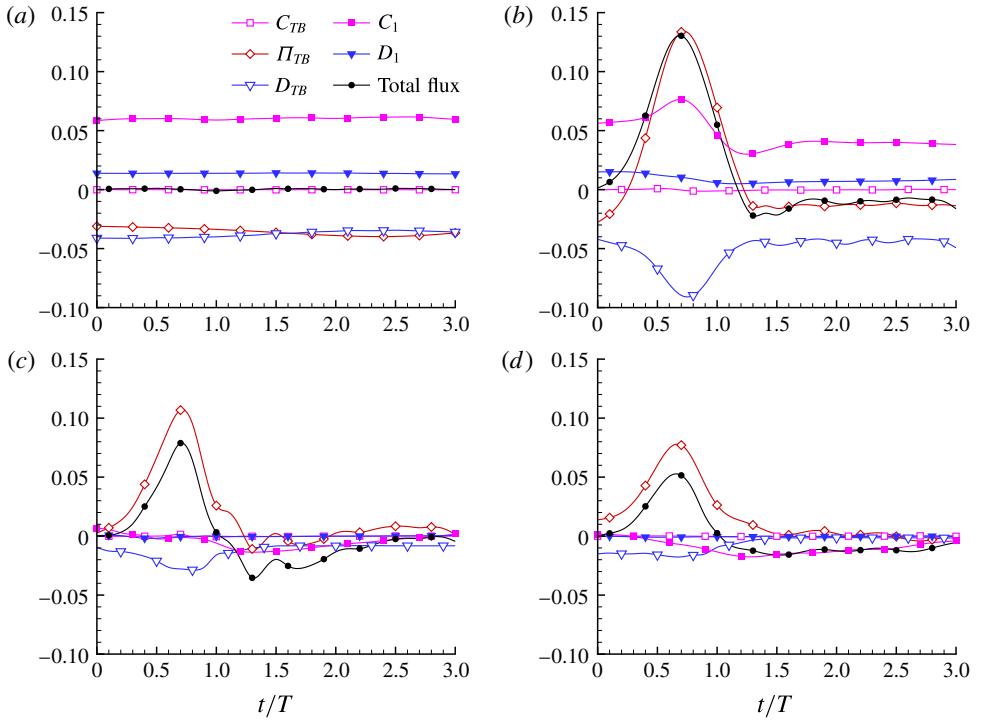


FIGURE 10. (Colour online) Time history of momentum fluxes across the top bound of wave surfaces and horizontal plane at z_1 in cases (*a*) A35, (*b*) A55, (*c*) B55 and (*d*) C55.

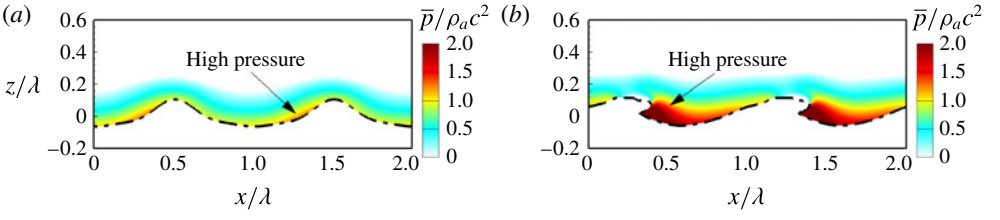


FIGURE 11. (Colour online) Phase-averaged pressure field near the wave surface in case A55 at (*a*) $t = 0.0T$ and (*b*) $t = 0.6T$. The pressure is normalized by $\rho_a c^2$. The thick dashed-dotted line represents the top bound of wave surfaces (see § 4.2 for the definition). The waves propagate in the $+x$-direction.

explore the physical process responsible for the increase of the pressure flux across the wave surface, we compare the ensemble-averaged pressure at $t = 0.0T$ and $t = 0.6T$ in case A55 in figure 11. It can be observed that at $t = 0.0T$, the pressure on the windward is higher than that on the leeward, which results in a form drag on the wind over steep waves. When the overturning jet is formed at $t = 0.6T$, as shown in figure 11(*b*), the pressure on the leeward increases significantly. This can be explained by the fact that the overturning jet increases the air pressure significantly to push the downstream air to move forward (see also figure 7*b*1). The pressure field demonstrated in figure 11(*b*) explains why the pressure flux changes its sign to become positive during wave plunging.

https://doi.org/10.1017/jfm.2018.466 Published online by Cambridge University Press

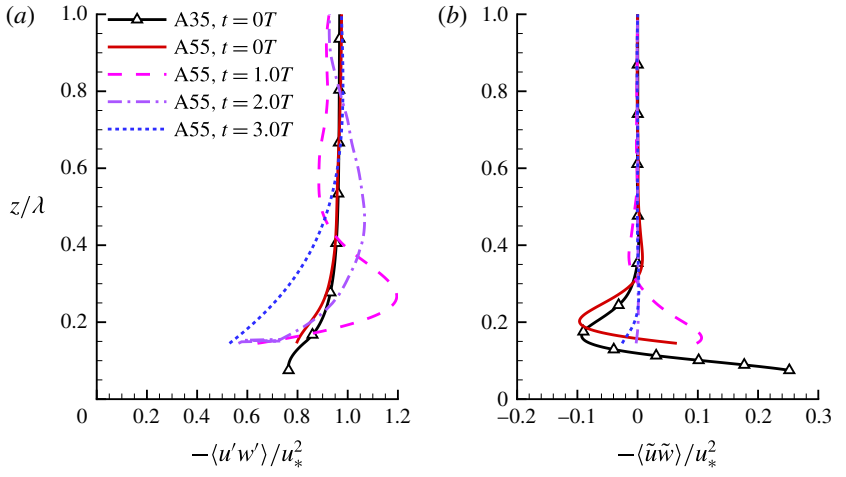


FIGURE 12. (Colour online) Vertical profiles of (*a*) plane-averaged total momentum flux $-\langle u'w'\rangle/u_*^2$ and (*b*) wave-coherent momentum flux $-\langle \tilde{u}\tilde{w}\rangle/u_*^2$ in case A55 at $t = 0.0T$, $1.0T$, $2.0T$ and $3.0T$. The result of case A35 at $t = 0.0T$ is plotted for comparison.

At the horizontal plane z_1, both the convection flux C_1 and viscous flux D_1 are positive in case A55 (figure 10*b*), indicating that the air near the wave surface gains momentum from the air above this plane. The magnitude of D_1 decreases after the wave breaking, consistent with the observation from figure 6(*b*) that the vertical gradient of mean velocity $\partial\langle u\rangle/\partial z$ decreases during wave breaking in case A55. The magnitude of C_1 also decreases, indicating that the turbulence is suppressed there. Figure 10(*c*,*d*) shows respectively that in cases B55 and C55, D_1 is relatively small compared with the other fluxes. The value of C_1 is positive before wave breaking, characterizing a downward momentum flux. However, C_1 becomes negative at $t = 0.8T$ and $t = 0.3T$ in cases B55 and C55, respectively, indicating that the mean momentum gained from the pressure flux at the top bound of wave surfaces is transported to higher altitudes.

4.5. *Momentum flux*

The plane-averaged total momentum flux $-\langle u'w'\rangle$ plays an important role in the evolution of the plane-averaged mean streamwise velocity, of which the governing equation reads

$$\frac{\partial\langle u\rangle}{\partial t} = \nu\frac{\partial^2\langle u\rangle}{\partial z^2} - \frac{\partial\langle u'w'\rangle}{\partial z}. \tag{4.4}$$

Figure 12 compares the profiles of $-\langle u'w'\rangle$ and its wave-coherent part $-\langle \tilde{u}\tilde{w}\rangle$ in case A55. The result of case A35 at $t = 0.0T$ is superimposed for comparison. At $t = 0.0T$, the profiles of $-\langle u'w'\rangle$ in cases A35 and A55 are close to each other, especially in the region away from the wave surface. As introduced in § 3, the initial field of the simulation is the fully developed wind turbulence over prescribed waves. In this statistically steady flow field, the left-hand side of (4.4) is trivial, and as a result, equation (4.4) can be further simplified to

$$\nu\frac{\partial\langle u\rangle}{\partial z} - \langle u'w'\rangle = u_*^2. \tag{4.5}$$

https://doi.org/10.1017/jfm.2018.466 Published online by Cambridge University Press

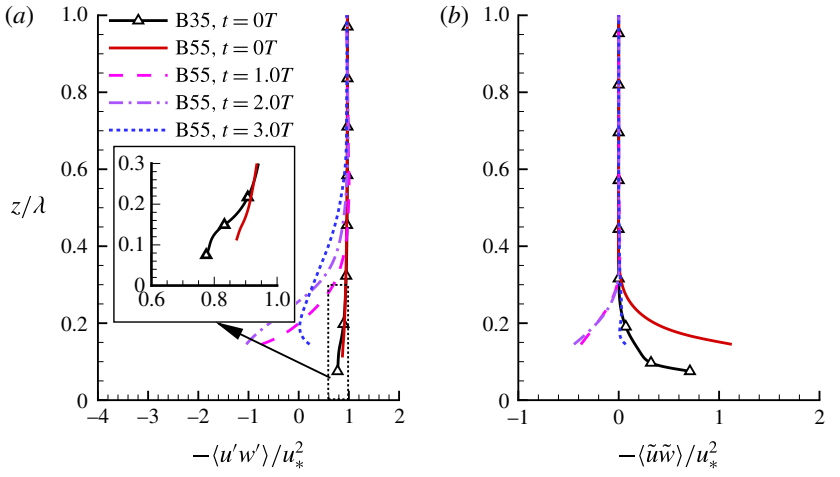


FIGURE 13. (Colour online) Vertical profiles of (*a*) plane-averaged total momentum flux $-\langle u'w'\rangle/u_*^2$ and (*b*) wave-coherent momentum flux $-\langle\tilde{u}\tilde{w}\rangle/u_*^2$ in case B55 at $t=0.0T$, $1.0T$, $2.0T$ and $3.0T$. The result of case B35 at $t=0.0T$ is plotted for comparison.

Figure 6(*b*) shows that $\partial\langle u\rangle/\partial z$ decreases as z/λ increases and becomes negligibly small far away from the wave surface. Therefore, as expected, it is observed from figure 12(*a*) that the value of $-\langle u'w'\rangle/u_*^2$ at $t=0.0T$ increases and approaches 1.0 as z/λ increases. This trend is consistent with the results of wind over non-breaking young waves in the literature (e.g. Sullivan *et al.* 2000; Yang & Shen 2010; Druzhinin *et al.* 2012; Sullivan *et al.* 2014).

The first plunging event disturbs the air near the wave surface, in a peak in the profile of $-\langle u'w'\rangle$ near $z/\lambda=0.27$ at $t=1.0T$ (figure 12*a*). Below and above this peak, the value of $-\partial\langle u'w'\rangle/\partial z$ is positive and negative, respectively. Because the viscous shear stress is less important than $-\langle u'w'\rangle$ in this region, it is understood from (4.4) that during wave breaking, the wind speed $\langle u\rangle$ is accelerated and decelerated below and above the peak of $-\langle u'w'\rangle$, respectively. The peak of $-\langle u'w'\rangle$ moves upward with its magnitude decreasing after $t=1.0T$, leading to an expansion of the acceleration region. As a result, the mean velocity increases after $t=1.0T$ (figure 6*b*).

Figure 12(*b*) shows that at $t=0.0T$, the value of $-\langle\tilde{u}\tilde{w}\rangle$ is positive near the wave crest height in case A55. It becomes negative above $z/\lambda=0.15$, and diminishes away from the wave surface ($z/\lambda>0.3$), indicating that the wave-coherent motion is confined in the near-surface region. At $t=1.0T$, the value of $-\langle\tilde{u}\tilde{w}\rangle$ above the wave crest becomes positive. After $t=2.0T$, the magnitude of $-\langle\tilde{u}\tilde{w}\rangle$ becomes negligibly small. Although the profile of $-\langle\tilde{u}\tilde{w}\rangle$ experiences a drastic change during wave breaking in case A55, it should not be regarded as the main reason for the occurrence of the peak in the profile of $-\langle u'w'\rangle$, because the magnitude of $-\langle\tilde{u}\tilde{w}\rangle$ is much smaller than that of $-\langle u'w'\rangle$. In the presence of wave plunging, the turbulence momentum flux (or, Reynolds stress) plays a much more important role than the wave-coherent momentum flux.

Figures 13 and 14 show the vertical profiles of $-\langle u'w'\rangle$ and $-\langle\tilde{u}\tilde{w}\rangle$ in cases B55 and C55, respectively. At $t=0.0T$, the value of $-\langle u'w'\rangle$ near the wave surface is larger in cases B55 and C55 than in cases B35 and C35, respectively. In case C55, the value of $-\langle u'w'\rangle/u_*^2$ is larger than 1.0 below $z/\lambda=0.30$ (figure 14*a*). According to equation (4.5), this indicates that the value of $\partial\langle u\rangle/\partial z$ is negative, which is consistent

https://doi.org/10.1017/jfm.2018.466 Published online by Cambridge University Press

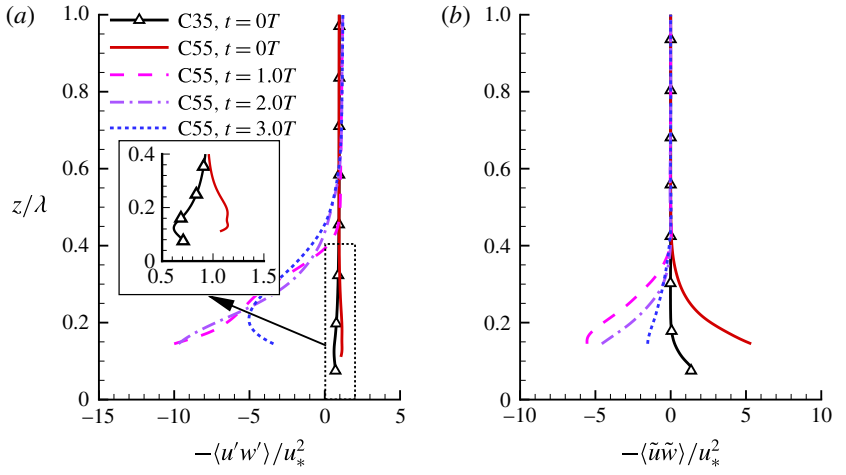


FIGURE 14. (Colour online) Vertical profiles of (*a*) plane-averaged total momentum flux $-\langle u'w'\rangle/u_*^2$ and (*b*) wave-coherent momentum flux $-\langle\tilde{u}\tilde{w}\rangle/u_*^2$ in case C55 at $t=0.0T$, $1.0T$, $2.0T$ and $3.0T$. The result of case C35 at $t=0.0T$ is plotted for comparison.

with the observation from figure 6(*d*). At $t=1.0T$, the value of $-\langle u'w'\rangle$ becomes negative in both cases B55 and C55. As discussed in § 4.4, this corresponds to the transport of momentum from the vicinity of the wave surface to the region away from the wave surface. At $t=3.0T$, the value of $-\partial\langle u'w'\rangle/\partial z$ is negative below $z/\lambda=0.2$ in cases B55 and C55. According to (4.4), this tends to decelerate the wind speed $\langle u\rangle$ near the wave surface, which is consistent with the results shown in figure 6(*c*,*d*).

A comparison among figures 12–14 indicates that the wave-coherent momentum flux $-\langle\tilde{u}\tilde{w}\rangle$ plays a more important role in cases B55 and C55 than in case A55. As shown in figure 13(*b*), the profile of $-\langle u'w'\rangle$ features a similar shape to that of $-\langle\tilde{u}\tilde{w}\rangle$ at $t=1.0T$ and $2.0T$ in case B55. In case C55, the contribution of $-\langle\tilde{u}\tilde{w}\rangle$ is more dominant. As shown in figure 14, the value of $-\langle\tilde{u}\tilde{w}\rangle/u_*^2$ is larger than 1.0 below $z/\lambda=0.3$. In response, the value of $-\langle u'w'\rangle/u_*^2$ also becomes larger than 1.0 in this region, which in turn leads to the negative value of $\partial\langle u\rangle/\partial z$ near the wave surface as shown in figure 6(*d*). At $t=1.0T$ and $2.0T$, the magnitude of $-\langle\tilde{u}\tilde{w}\rangle$ is comparable to that of $-\langle u'w'\rangle$ in case C55, indicating that the evolution of $-\langle u'w'\rangle$ is dominated by the wave-coherent motion, when the wave age is large.

Figure 15 displays the contours of the ensemble-averaged Reynolds shear stress $-\overline{u''w''}$ near the wave surface in case A55. We recall here that the thick dashed-dotted line is the top bound of the wave surfaces, which is different from instantaneous wave surface. The definition of top bound of wave surface is given in § 4.2, and the top bound of the wave surfaces and instantaneous wave surface are compared in figures 7–9. Figure 15(*a*) shows that at $t=0.0T$, the value of $-\overline{u''w''}$ is negative in a thin layer attached to the windward of the wave surface. Above this layer, $-\overline{u''w''}$ is positive, and a peak is located to the upper left of the windward of the wave surface. At $t=0.8T$, the coherent vortex to the right of the wave crest enhances the momentum flux around it, and as a result, a large magnitude of $-\overline{u''w''}$ is observed around the vortex in figure 15(*b*). From the comparison between figure 15(*a*,*c*), it is known that the magnitude of $-\overline{u''w''}$ is smaller at $t=3.0T$ than at $t=0.0T$, indicating that the turbulence is reduced after wave plunging. This is consistent with the results of the plane-averaged total momentum flux demonstrated in figure 12(*a*).

https://doi.org/10.1017/jfm.2018.466 Published online by Cambridge University Press

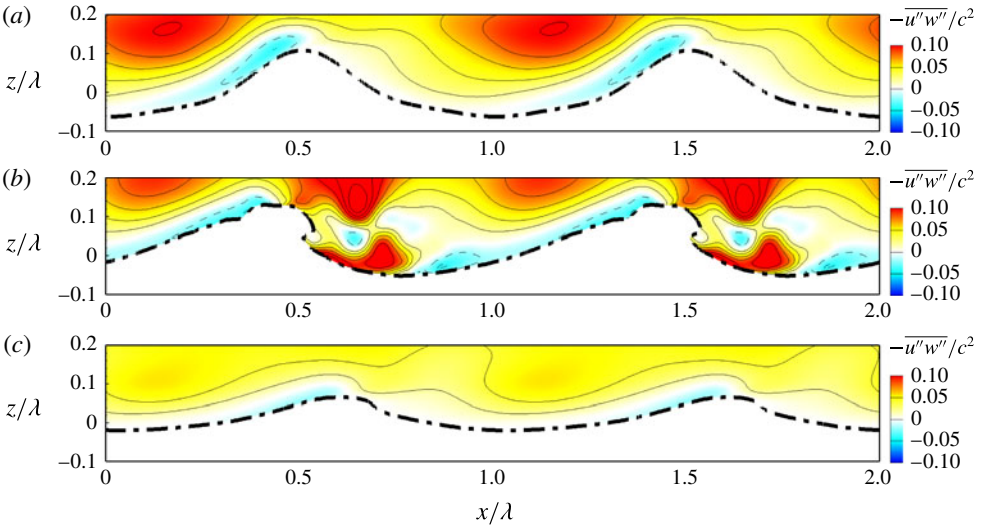


FIGURE 15. (Colour online) Contours of ensemble-averaged Reynolds shear stress $-\overline{u''w''}/c^2$ at (*a*) $t=0.0T$, (*b*) $t=0.8T$ and (*c*) $t=3.0T$ in case A55. The solid and dashed lines represent isopleths of positive and negative values of $-\overline{u''w''}/c^2$, respectively. The interval of the isopleths is 0.02. The thick dashed-dotted line represents the top bound of the wave surfaces (see § 4.2 for the definition). The waves propagate in $+x$ direction.

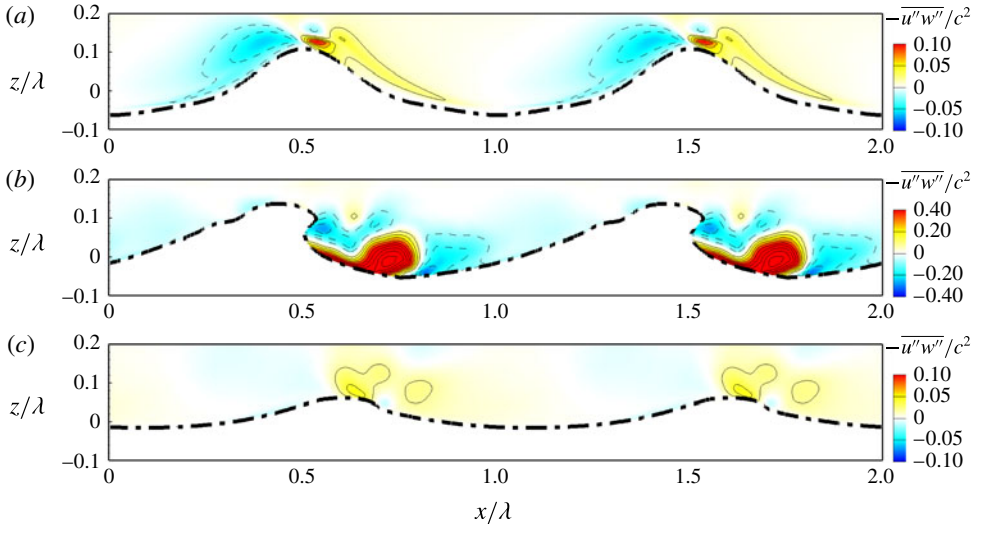


FIGURE 16. (Colour online) Contours of ensemble-averaged Reynolds shear stress $-\overline{u''w''}/c^2$ at (*a*) $t=0.0T$, (*b*) $t=0.8T$ and (*c*) $t=3.0T$ in case B55. See figure 15 for the detailed caption.

Figures 16 and 17 display the contours of the ensemble-averaged Reynolds shear stress $-\overline{u''w''}$ near the wave surface in cases B55 and C55, respectively. From the comparison among figures 15(*a*), 16(*a*) and 17(*a*), it can be seen that at $t=0.0T$, the region with negative $-\overline{u''w''}$ on the windward of the wave expands as c/u_* increases,

https://doi.org/10.1017/jfm.2018.466 Published online by Cambridge University Press

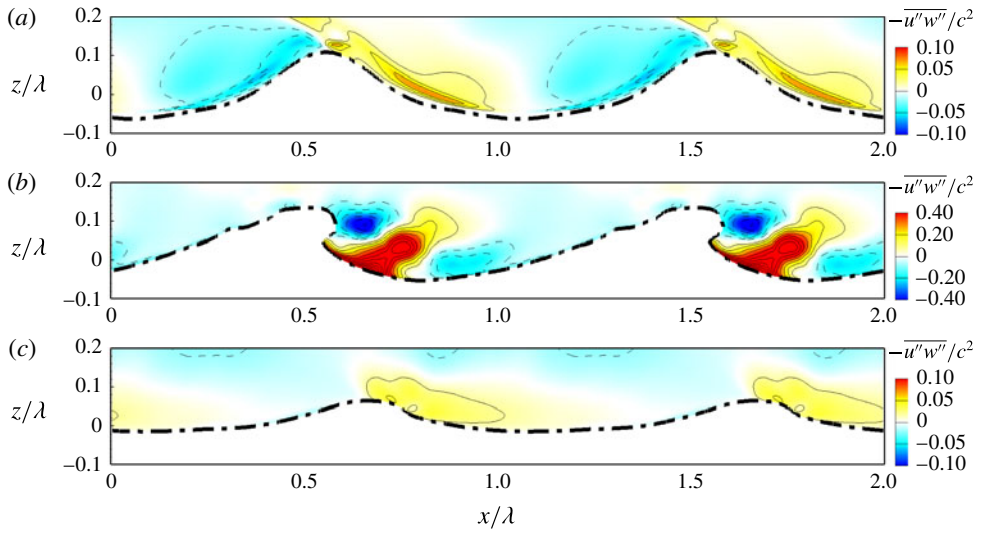


FIGURE 17. (Colour online) Contours of ensemble-averaged Reynolds shear stress $-\overline{u''w''}/c^2$ at (*a*) $t = 0.0T$, (*b*) $t = 0.8T$ and (*c*) $t = 3.0T$ in case C55. See figure 15 for the detailed caption.

and the positive and negative contours become more symmetric about the wave crest. The same trend of the ensemble-averaged Reynolds stress contours in response to the increase of c/u_* has been reported by Yang & Shen (2010) for wind over non-breaking waves. Similar to that in case A55 (figure 15*b*), the spanwise vortex induces large magnitude of $-\overline{u''w''}$ around it at $t = 0.8T$ in cases B55 and C55 (figures 16*b* and 17*b*). The comparisons between figure 16(*a*,*c*) and between 17(*a*,*c*) show that the magnitude of $-\overline{u''w''}$ is slightly smaller at $t = 3.0T$ than at $t = 0.0T$ in both cases B55 and C55, indicating the reduction of turbulence after wave breaking. This is consistent with case A55 for young waves (figure 15*a*,*c*).

4.6. *Kinetic energy of velocity fluctuations*

In this section, we further analyse the effect of wave breaking on the kinetic energy of velocity fluctuations (KE-F). Figures 18–20 compare the vertical profiles of the plane-averaged KE-F, $k_{pl} = \langle u_i' u_i' \rangle/2$, and the kinetic energy of wave-coherent velocity (KE-W), $k_w = \langle \tilde{u}_i \tilde{u}_i \rangle/2$, in cases with young waves (A35 and A55), intermediate waves (B35 and B55) and old waves (C35 and C55), respectively.

From the comparison between (*a*,*b*) in figures 18–20, it is known that the contribution from k_w to k_{pl} becomes more important as the wave age increases, consistent with the results of $-\langle u'w' \rangle$ and $-\langle \tilde{u}\tilde{w} \rangle$ displayed in figures 12–14. The wave steepness influences both k_{pl} and k_w near the wave surface. As shown in figures 18–20, at $t = 0.0T$, the magnitudes of k_{pl} and k_w in cases A55, B55 and C55 are respectively larger than those in cases A35, B35 and C35 below $z/\lambda = 0.4$. However, the wave steepness does not influence the KE-F far away from the wave surface. This is consistent with the results of the mean velocity and total momentum flux demonstrated in figures 6, 12–14.

The wave plunging influences the KE-F near the wave surface significantly. As shown in figure 18(*a*), in case A55, the value of k_{pl} below $z/\lambda = 0.55$ is higher at $t =$

https://doi.org/10.1017/jfm.2018.466 Published online by Cambridge University Press

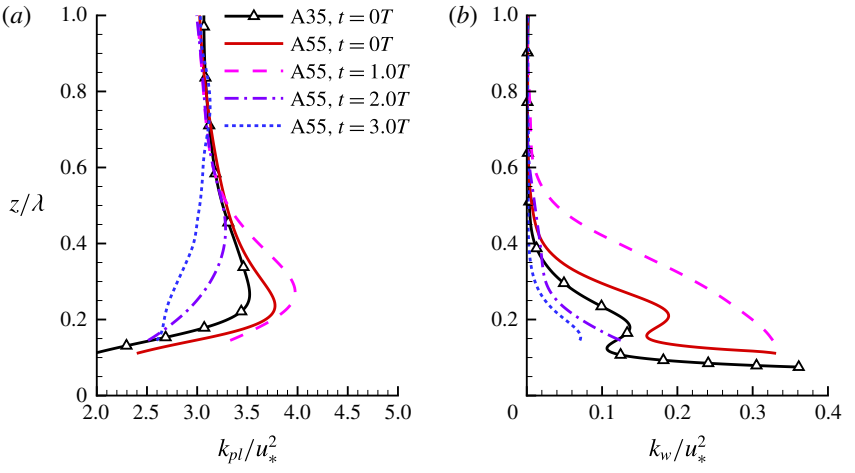


FIGURE 18. (Colour online) Vertical profiles of (*a*) plane-averaged KE-F k_{pl}/u_*^2 and (*b*) KE-W k_w/u_*^2 in case A55 at $t = 0.0T$, $1.0T$, $2.0T$ and $3.0T$. The result of case A35 at $t = 0.0T$ is plotted for comparison.

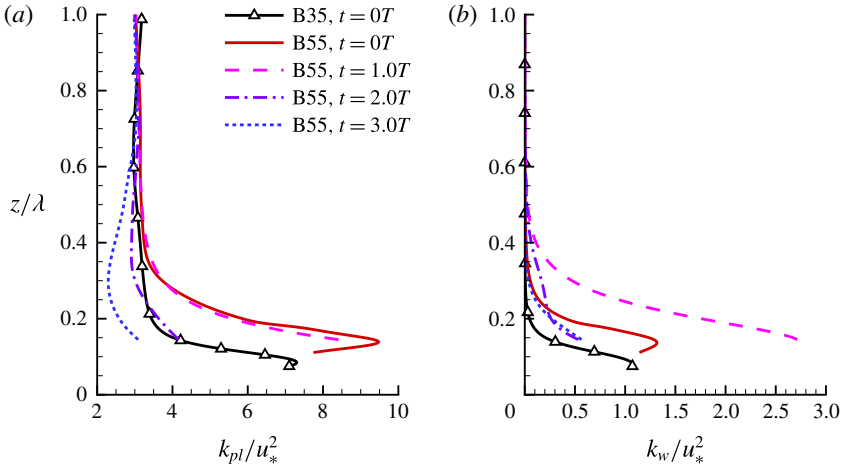


FIGURE 19. (Colour online) Vertical profiles of (*a*) plane-averaged KE-F k_{pl}/u_*^2 and (*b*) KE-W k_w/u_*^2 in case B55 at $t = 0.0T$, $1.0T$, $2.0T$ and $3.0T$. The result of case B35 at $t = 0.0T$ is plotted for comparison.

$1.0T$ than at $t = 0.0T$, indicating that the turbulence is transiently enhanced due to the wave breaking. The KE-F also experiences a transient growth in case C55. However, we do not observe such a transient growth of KE-F in case B55. The turbulence is eventually reduced after wave plunging ceases in cases A55, B55 and C55.

To further study why the transient growth of KE-F takes place in cases A55 and C55 but is absent in case B55, we compare the production of KE-F, P_k, in these three cases in figure 21. Here, P_k is defined as

$$P_k = -\langle u'w' \rangle \frac{\partial \langle u \rangle}{\partial z}. \tag{4.6}$$

https://doi.org/10.1017/jfm.2018.466 Published online by Cambridge University Press

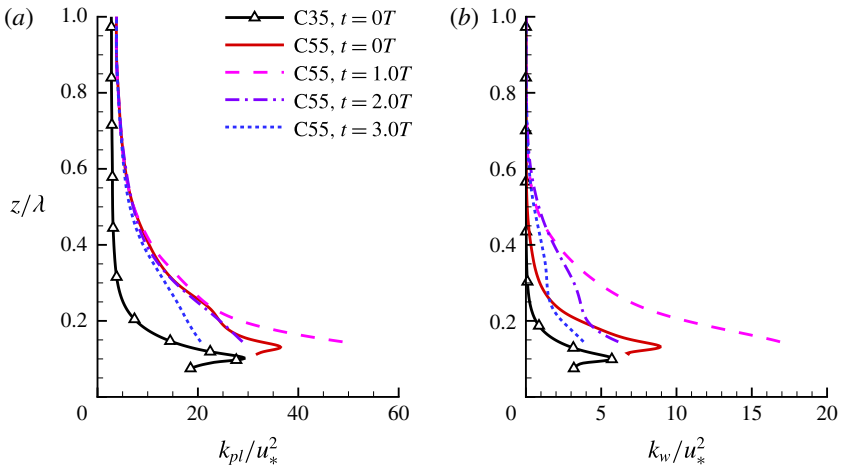


FIGURE 20. (Colour online) Vertical profiles of (*a*) plane-averaged KE-F k_{pl}/u_*^2 and (*b*) KE-W k_w/u_*^2 in case C55 at $t = 0.0T$, $1.0T$, $2.0T$ and $3.0T$. The result of case C35 at $t = 0.0T$ is plotted for comparison.

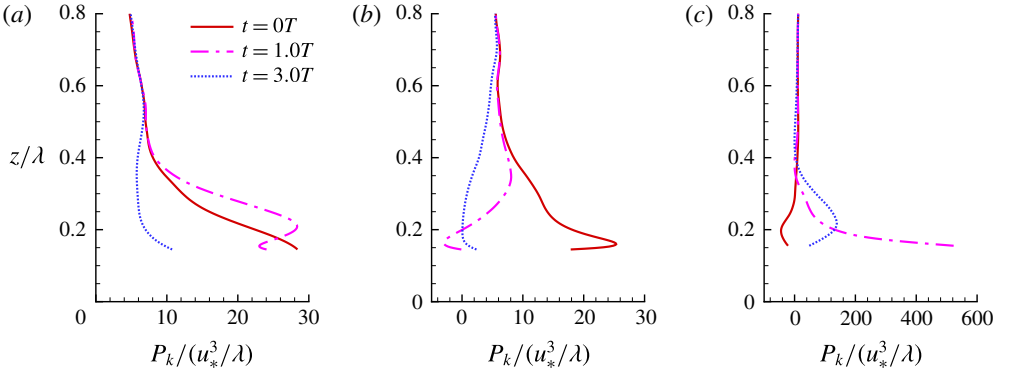


FIGURE 21. (Colour online) Vertical profile of plane-averaged KE-F production $P_k/(u_*^3/\lambda)$ in cases (*a*) A55, (*b*) B55 and (*c*) C55.

The production term represents a rapid effect on the KE-F (Townsend 1980), and the behaviour of KE-F is often dominated by its production term (Mansour, Kim & Moin 1988; Smits, McKeon & Marusic 2011). Note that the full production term of KE-F reads

$$P_k = -\langle u_i' u_j' \rangle \frac{\partial \langle u_i \rangle}{\partial x_j}. \tag{4.7}$$

However, according to the definition of plane averaging, $\partial\langle\ \rangle/\partial x = \partial\langle\ \rangle/\partial y = 0$ holds theoretically. Furthermore, the magnitudes of the mean spanwise velocity $\langle v \rangle$ and mean vertical velocity $\langle w \rangle$ are negligibly small in comparison with the mean streamwise velocity $\langle u \rangle$. As a result, the production of KE-F is simplified to (4.6).

It is evident from figure 21(*a*,*c*) that in cases A55 and C55, the magnitude of P_k is larger at $t = 1.0T$ than at $t = 0.0T$. However, the physical process leading to the

https://doi.org/10.1017/jfm.2018.466 Published online by Cambridge University Press

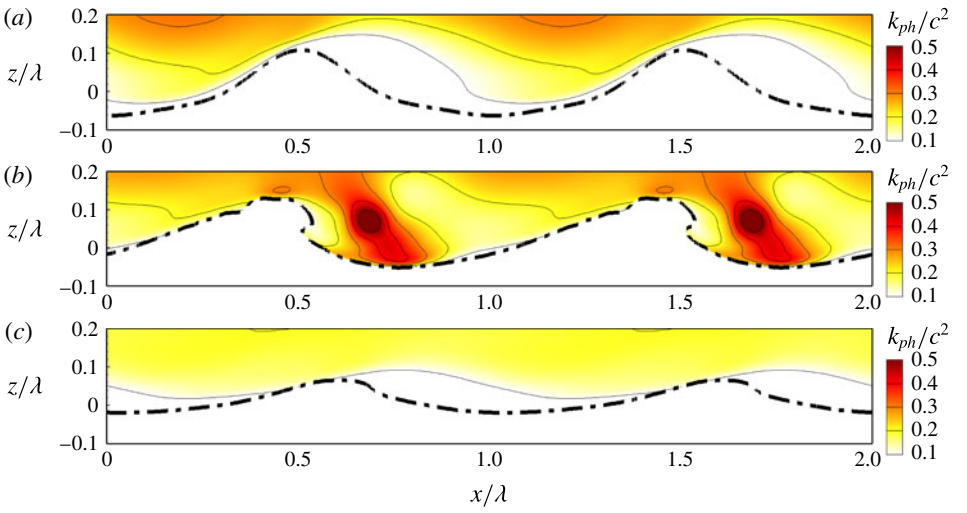


FIGURE 22. (Colour online) Contours of ensemble-averaged TKE, k_{ph}/c^2, at (*a*) $t = 0.0T$, (*b*) $t = 0.8T$ and (*c*) $t = 3.0T$ in case A55. The interval of the isopleths is 0.1. The thick dashed-dotted line represents the top bound of wave surfaces (see § 4.2 for the definition). The waves propagate in the $+x$-direction.

increase of P_k is different in these two cases. From equation (4.6), it is known that the value of P_k is determined by the vertical gradient of mean velocity $\partial\langle u\rangle/\partial z$ and the total momentum flux $-\langle u'w'\rangle$. In case A55, $\partial\langle u\rangle/\partial z$ decreases during the first plunging event (as can be seen from the $\langle u\rangle$ profile in figure 6*b*), which tends to reduce the value of P_k. On the opposite, the magnitude of $-\langle u'w'\rangle$ increases and a positive peak occurs in its profile (figure 12*a*) due to the disturbance effect of the wave breaking on the turbulent flow, which tends to cause an increase of P_k. Figure 21(*a*) indicates that the latter effect is stronger in the young wave case, and as a result k_{pl} experiences a transient growth during the first plunging event (figure 18*a*). In case C55, the transient growth of KE-F is correlated to the negative value of $\partial\langle u\rangle/\partial z$ near the wave surface (figure 6*d*), which leads to a negative value of P_k at $t = 0.0T$ as shown in figure 21(*c*). During the first plunging event, because the wave breaking induces a large negative value of $-\langle\tilde{u}\tilde{w}\rangle$ (figure 14*b*), the value of $-\langle u'w'\rangle$ becomes negative correspondingly (figure 14*a*). As a result, P_k becomes positive at $t = 1.0T$ near the wave surface. Consequently, the magnitude of KE-F also increases transiently in case C55 during the first plunging event. In case B55, however, none of the two processes described above is present. As demonstrated in figure 13(*a*), no positive peak occurs in the profile of $-\langle u'w'\rangle$ during the first plunging event, while figure 6(*c*) shows that $\partial\langle u\rangle/\partial z$ is positive in case B55. Therefore, the turbulence does not experience a transient growth in this intermediate wave case. The production of KE-F is smaller at $t = 3.0T$ than at $t = 1.0T$ in all cases, which leads to the magnitude decrease of KE-F after wave plunging (figures 18*a*, 19*a* and 20*a*).

Figure 22 displays the contours of the ensemble-averaged TKE, $k_{ph} = \overline{u_i''u_i''}/2$, near the wave surface in case A55. As shown in figure 22(*a*), at $t = 0.0T$, the value of k_{ph} is small near the leeward of the surface. Figure 22(*b*) shows that at $t = 0.8T$, k_{ph} increases near the large spanwise vortex (cf. figure 7*c*3), indicating that the turbulence is enhanced by the vortex. This is consistent with the result of $-\overline{u''w''}$ shown in

https://doi.org/10.1017/jfm.2018.466 Published online by Cambridge University Press

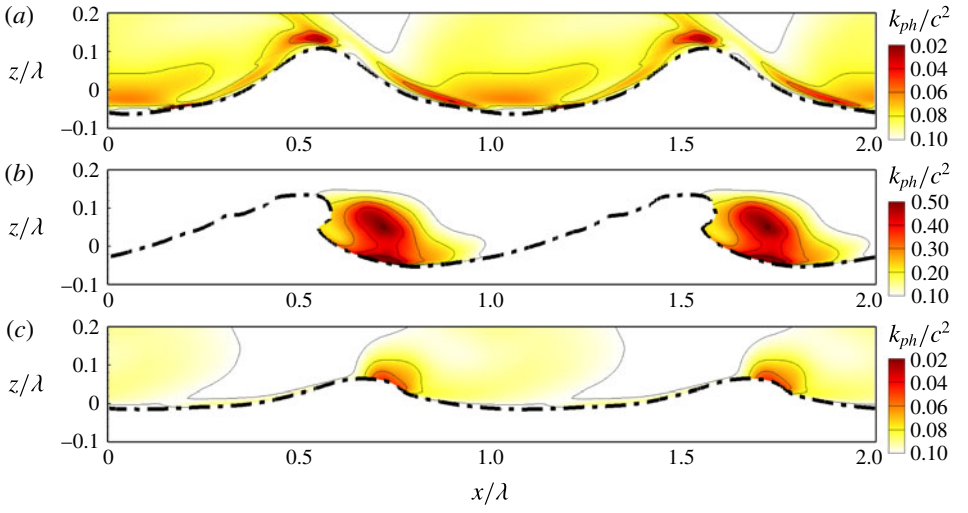


FIGURE 23. (Colour online) Contours of ensemble-averaged TKE, k_{ph}/c^2, at (*a*) $t = 0.0T$, (*b*) $t = 0.8T$ and (*c*) $t = 3.0T$ in case C55. The interval of isopleths is 0.02 in (*a*,*c*), while it is 0.1 in (*b*). The thick dashed-dotted line represents the top bound of wave surfaces (see § 4.2 for the definition). The waves propagate in the $+x$-direction.

figure 15(*b*). At $t = 3.0T$, as the turbulence is reduced, the magnitude of k_{ph} is smaller than that at $t = 0.0T$.

Figure 23 illustrates the contours of k_{ph} near the wave surface in case C55. As shown in figure 23(*a*), the peak of k_{ph} occurs near the wave surface at $t = 0.0T$. Similar to that in case A55, the magnitude of k_{ph} increases significantly at $t = 0.8T$ near the spanwise vortex (cf. figure 9*b*3). The value of k_{ph} near the vortex at $t = 0.8T$ scales with c^2 in cases A55 and C55, indicating that the high TKE in this region is dominated by the wave breaking. At $t = 3.0T$, the magnitude of k_{ph} near the wave surface becomes smaller than that at $t = 0.0T$. This is similar to the results of case A55 shown in figure 22.

The figures of k_{ph} of case B55 are not shown here to keep the paper concise. Similar to that in cases A55 and C55, the magnitude of TKE in case B55 experiences an increase during the wave plunging near the wave surface, and is eventually reduced after the wave breaking. However, the TKE far away from the wave surface does not increase transiently in case B55 during wave plunging (figure 19*a*). This indicates that although TKE is generated in the vicinity of the wave surface during wave plunging, little is transported to high altitude before it is dissipated. As shown above, the transient growth of KE-F away from the wave surface during wave plunging in cases A55 and C55 is caused by the large magnitude of local KE-F production.

5. Conclusions

In this study, direct numerical simulations are performed to study wind over breaking waves. The air and water are simulated as a coherent system, with the interfaced captured using the coupled level-set and volume-of-fluid method. Three wave ages and two initial wave steepness values are considered. Because wave breaking is an unsteady process, we conduct 100 runs for each case to perform

https://doi.org/10.1017/jfm.2018.466 Published online by Cambridge University Press

ensemble averaging, of which the initial wind profile and wave geometry are the same, while the instantaneous turbulent fluctuations are different.

It is found that before wave breaking, the turbulence statistics are significantly influenced by the wave age. The vertical gradient of mean velocity is positive at small and medium wave ages, but at the large wave age, it becomes negative near the wave surface. This is because the pressure force changes from drag to thrust as the wave age increases. The contribution of the wave-induced motion to the total momentum flux and KE-F is relatively small at the small wave age, indicating that the flow physics of the airflow is dominated by the wind turbulence. In contrast, contribution of the wave-induced part becomes increasingly important as the wave age increases.

Wave spilling does not alter the wind turbulence significantly. In contrast, wave plunging induces substantial effects on the turbulence statistics and flow structures near the wave surface. During wave plunging, the overturning jet pushes the air to accelerate it in the streamwise direction. The pressure near the impinging jet increases significantly, leading to the momentum flux from water to air, which is in the opposite direction to that before wave breaking, when the steep wave exerts drag on the airflow. As a result, the wind speed near the wave surface is accelerated by the breaker. Meanwhile, a spanwise vortex rotating in the counterclockwise direction is generated, of which the streamwise extent increases as the wave age increases. The airflow near this large vortex is greatly disturbed, and in consequence, the magnitudes of the Reynolds shear stress and TKE near this large vortex are significantly amplified. At the small wave age, the turbulence above the wave crest experiences a transient enhancement during the first plunging event, which is characterized by the transient growth of the magnitude of KE-F. A further investigation of the KE-F production shows that this is caused by the peak occurring in the profile of the total momentum flux due to the disturbance effect of wave plunging. At the large wave age, the KE-F above the wave crest also increases during wave plunging. This is because the sign of the KE-F production changes from negative to positive during wave plunging, which results from the change in the sign of the wave-coherent momentum flux. Therefore, the processes leading to the transient increases of KE-F at small and large wave ages are different. At the intermediate wave age, both processes are absent, and no transient growth of KE-F is observed.

Finally, we remark that while the results shown in this paper indicate that DNS is a useful tool for mechanistic studies of small-scale physical processes associated with wind over breaking waves, it would be desirable to perform fine-resolution simulation of more realistic problems with the increase of computer power in the future. For example, the wave-focusing method might be used to generate breaking waves under the wind, such that the historical effect of wind on the wave geometry can be captured. This imposes a higher demand on the computing power, because the computational domain size needs to be significantly elongated in the streamwise direction. Furthermore, it would be desirable to assimilate laboratory and field measurement data into the simulation to help the set-up of more realistic simulations. These research directions will be the pursuits in our future studies.

Acknowledgements

This work is supported by Office of Naval Research and Minnesota Sea Grant. The authors would like to thank Professors J. Duncan and F. Veron for the helpful discussion on the results.

https://doi.org/10.1017/jfm.2018.466 Published online by Cambridge University Press

REFERENCES

BABANIN, A. 2011 *Breaking and Dissipation of Ocean Surface Waves*. Cambridge University Press.

BABANIN, A., CHALIKOV, D., YOUNG, I. & SAVELYEV, I. 2007 Predicting the breaking onset of surface water waves. *Geophys. Res. Lett.* **34**, L07605.

BABANIN, A. V., CHALIKOV, D., YOUNG, I. R. & SAVELYEV, I. 2010 Numerical and laboratory investigation of breaking of steep two-dimensional waves in deep water. *J. Fluid Mech.* **644**, 433–463.

BALAY, S., GROPP, W. D., MCINNES, L. C. & SMITH, B. F. 1997 Efficient management of parallelism in object oriented numerical software libraries. In *Modern Software Tools in Scientific Computing* (ed. E. Arge, A. M. Bruaset & H. P. Langtangen), pp. 163–202. Birkhäuser.

BANNER, M. L. 1990 The influence of wave breaking on the surface pressure distribution in wind–wave interactions. *J. Fluid Mech.* **211**, 463–495.

BANNER, M. L. & MELVILLE, W. K. 1976 On the separation of air flow over water waves. *J. Fluid Mech.* **77**, 825–842.

BANNER, M. L. & PEIRSON, W. L. 1998 Tangential stress beneath wind-driven air–water interfaces. *J. Fluid Mech.* **364**, 115–145.

BANNER, M. L. & PEIRSON, W. L. 2007 Wave breaking onset and strength for two-dimensional deep-water wave groups. *J. Fluid Mech.* **585**, 93–115.

BANNER, M. L. & PEREGRINE, D. H. 1993 Wave breaking in deep water. *Annu. Rev. Fluid Mech.* **25**, 373–397.

BANNER, M. L. & TIAN, X. 1998 On the determination of the onset of breaking for modulating surface gravity water waves. *J. Fluid Mech.* **367**, 107–137.

BELCHER, S. E. & HUNT, J. C. R. 1998 Turbulent flow over hills and waves. *Annu. Rev. Fluid Mech.* **30**, 507–538.

BELL, M. M., MONTGOMERY, M. T. & EMANUEL, K. A. 2012 Air–sea enthalpy and momentum exchange at major hurricane wind speeds observed during CBLAST. *J. Atmos. Sci.* **69**, 3197–3222.

BLENKINSOPP, C. E. & CHAPLIN, J. R. 2007 Void fraction measurements in breaking waves. *Proc. R. Soc. Lond.* A **463**, 3151–3170.

BONMARIN, P. 1989 Geometric properties of deep-water breaking waves. *J. Fluid Mech.* **209**, 405–433.

BONMARIN, P. & RAMAMONJIARISOA, A. 1985 Deformation to breaking of deep water gravity waves. *Exp. Fluids* **3**, 11–16.

BROCCHINI, M. & PEREGRINE, D. H. 2001 The dynamics of strong turbulence at free surfaces. Part 2. Free-surface boundary conditions. *J. Fluid Mech.* **449**, 255–290.

BUCKLEY, M. P. & VERON, F. 2016 Structure of the airflow above surface waves. *J. Phys. Oceanogr.* **46**, 1377–1397.

CAULLIEZ, G. 2013 Dissipation regimes for short wind waves. *J. Geophys. Res.* **118** (2), 672–684.

CHANG, K.-A. & LIU, P. L.-F. 1998 Velocity, acceleration and vorticity under a breaking wave. *Phys. Fluids* **10** (1), 327–329.

CHASSAING, P., ANTONIA, R. A., ANSELMET, F., JOLY, L. & SARKAR, S. 2002 *Variable Density Fluid Turbulence*. Kluwer.

CHEN, G., KHARIF, C., ZALESKI, S. & LI, J. 1999 Two-dimensional Navier–Stokes simulation of breaking waves. *Phys. Fluids* **11** (1), 121–133.

CHIANG, W.-S. & HWUNG, H.-H. 2007 Steepness effect on modulation instability of the nonlinear wave train. *Phys. Fluids* **19** (1), 014105.

DEANE, G. B. & STOKES, M. D. 2002 Scale dependence of bubble creation mechanisms in breaking waves. *Nature* **418**, 839–844.

DEIKE, L., MELVILLE, W. K. & POPINET, S. 2016 Air entrainment and bubble statistics in breaking waves. *J. Fluid Mech.* **801**, 91–129.

DEIKE, L., POPINET, S. & MELVILLE, W. K. 2015 Capillary effects on wave breaking. *J. Fluid Mech.* **769**, 541–569.

DERAKHTI, M. & KIRBY, J. T. 2014 Bubble entrainment and liquid–bubble interaction under unsteady breaking waves. *J. Fluid Mech.* **761**, 464–506.

https://doi.org/10.1017/jfm.2018.466 Published online by Cambridge University Press

DERAKHTI, M. & KIRBY, J. T. 2016 Breaking-onset, energy and momentum flux in unsteady focused wave packets. *J. Fluid Mech.* **790**, 553–581.

DIORIO, J. D., LIU, X. & DUNCAN, J. H. 2009 An experimental investigation of incipient spilling breakers. *J. Fluid Mech.* **633**, 271–283.

DONELAN, M. A., HAUS, B. K., REUL, N., PLANT, W. J., STIASSNIE, M., GRABER, H. C., BROWN, O. B. & SALTZMAN, E. S. 2004 On the limiting aerodynamic roughness of the ocean in very strong winds. *Geophys. Res. Lett.* **31**, L18306.

DRAZEN, D. A., MELVILLE, W. K. & LENAIN, L. 2008 Inertial scaling of dissipation in unsteady breaking waves. *J. Fluid Mech.* **611**, 307–332.

DRUZHININ, O. A., TROITSKAYA, Y. I. & ZILITINKEVICH, S. S. 2012 Direct numerical simulation of a turbulent wind over a wavy water surface. *J. Geophys. Res.* **117**, C00J05.

DUNCAN, J. H. 1981 An experimental investigation of breaking waves produced by a towed hydrofoil. *Proc. R. Soc. Lond.* A **377**, 331–348.

DUNCAN, J. H. 1983 The breaking and non-breaking wave resistance of a two-dimensional hydrofoil. *J. Fluid Mech.* **126**, 507–520.

DUNCAN, J. H. 2001 Spilling breakers. *Annu. Rev. Fluid Mech.* **33**, 519–547.

DUNCAN, J. H., QIAO, H., PHILOMIN, V. & WENZ, A. 1999 Gentle spilling breakers: crest profile evolution. *J. Fluid Mech.* **379**, 191–222.

ESWARAN, V. & POPE, S. B. 1988 An examination of forcing in direct numerical simulations of turbulence. *Comput. Fluids* **16** (3), 257–278.

FEDOROV, A. V., MELVILLE, W. K. & ROZENBERG, A. 1998 An experimental and numerical study of parasitic capillary waves. *Phys. Fluids* **10** (6), 1315–1323.

HARA, T. & SULLIVAN, P. P. 2015 Wave boundary layer turbulence over surface waves in a strongly forced condition. *J. Phys. Oceanogr.* **45**, 868–883.

HENDRICKSON, K., WEYMOUTH, G., BANERJEE, S. & YUE, D. K.-P. 2013 Air entraiment and multiphase turbulence in the bubbly wake of a transom stern. *Int. Shipbuilding Progress* **60** (1–4), 375–401.

HOLTHUIJSEN, L. H., POWELL, M. D. & PIETRZAK, J. D. 2012 Wind and waves in extreme hurricanes. *J. Geophys. Res.* **117**, C09003.

HONG, W.-L. & WALKER, D. T. 2000 Reynolds-averaged equations for free-surface flows with application to high-Froude-number jet spreading. *J. Fluid Mech.* **417**, 183–209.

HSU, C.-T., HSU, E. Y. & STREET, R. L. 1981 On the structure of turbulent flow over a progressive water wave: theory and experiment in a transformed, wave-following co-ordinate system. *J. Fluid Mech.* **105**, 87–117.

HU, Y., GUO, X., LU, X., LIU, Y., DALRYMPLE, R. A. & SHEN, L. 2012 Idealized numerical simulation of breaking water wave propagating over a viscous mud layer. *Phys. Fluids* **24** (11), 112104.

IAFRATI, A. 2009 Numerical study of the effects of the breaking intensity on wave breaking flows. *J. Fluid Mech.* **622**, 371–411.

IAFRATI, A. 2011 Energy dissipation mechanisms in wave breaking processes: spilling and highly aerated plunging breaking events. *J. Geophys. Res.* **116**, C07024.

IAFRATI, A., BABANIN, A. & ONORATO, M. 2013 Modulational instability, wave breaking, and formation of large-scale dipoles in the atmosphere. *Phys. Rev. Lett.* **110**, 184504.

JAROSZ, E., MITCHELL, D. A., WANG, D. W. & TEAGUE, W. J. 2007 Bottom-up determination of air–sea momentum exchange under a major tropical cyclone. *Science* **315** (5819), 1707–1709.

JIANG, L., LIN, H.-J., SCHULTZ, W. W. & PERLIN, M. 1999 Unsteady ripple generation on steep gravity–capillary waves. *J. Fluid Mech.* **386**, 281–304.

JIANG, Q., SULLIVAN, P., WANG, S., DOYLE, J. & VINCENT, L. 2016 Impact of swell on air–sea momentum flux and marine boundary layer under low-wind conditions. *J. Atmos. Sci.* **73**, 2683–2697.

JOHANNESSEN, T. B. & SWAN, C. 2001 A laboratory study of the focusing of transient and directionally spread surface water waves. *Proc. R. Soc. Lond.* A **457**, 971–1006.

KAWAI, S. 1982 Structure of air flow separation over wind wave crests. *Boundary-Layer Meteorol.* **23**, 503–521.

https://doi.org/10.1017/jfm.2018.466 Published online by Cambridge University Press

KAWAMURA, H. & TOBA, Y. 1988 Ordered motion in the turbulent boundary layer over wind waves. *J. Fluid Mech.* **197**, 105–138.

KHARIF, C., GIOVANANGELI, J.-P., TOUBOUL, J., GRARE, L. & PELINOVSKY, E. 2008 Influence of wind on extreme wave events: experimental and numerical approaches. *J. Fluid Mech.* **594**, 209–247.

KIGER, K. T. & DUNCAN, J. H. 2012 Air-entrainment mechanisms in plunging jets and breaking waves. *Annu. Rev. Fluid Mech.* **44**, 563–596.

KIM, J. & MOIN, P. 1985 Application of a fractional-step method to incompressible Navier–Stokes equations. *J. Comput. Phys.* **59**, 308–323.

KUDRYAVTSEV, V. N. & MAKIN, V. K. 2001 The impact of air-flow separation on the drag of the sea surface. *Boundary-Layer Meteorol.* **98**, 155–171.

KUDRYAVTSEV, V. N. & MAKIN, V. K. 2007 Aerodynamic roughness of the sea surface at high winds. *Boundary-Layer Meteorol.* **125**, 289–303.

LAMARRE, E. & MELVILLE, W. K. 1991 Air entrainment and dissipation in breaking waves. *Nature* **351**, 469–472.

LAMB, H. 1932 *Hydrodynamics*. Cambridge University Press.

LIU, B., GUAN, C. & XIE, L. 2012 The wave state and sea spray related parameterization of wind stress applicable from low to extreme winds. *J. Geophys. Res.* **117**, C00J22.

LIU, X. & DUNCAN, J. H. 2003 The effects of surfactants on spilling breaking waves. *Nature* **421**, 520–523.

LIU, X. & DUNCAN, J. H. 2006 An experimental study of surfactant effects on spilling breakers. *J. Fluid Mech.* **567**, 433–455.

LIU, Y. 2012 Numerical study of strong free surface flow and breaking waves. PhD thesis, The Johns Hopkins University.

LONGUET-HIGGINS, M. & TANAKA, M. 1997*a* Crest instabilities of gravity waves. Part 3. Nonlinear development and breaking. *J. Fluid Mech.* **336**, 33–50.

LONGUET-HIGGINS, M. & TANAKA, M. 1997*b* On the crest instabilities of steep surface waves. *J. Fluid Mech.* **336**, 51–68.

LONGUET-HIGGINS, M. S. 1982 Parametric solutions for breaking waves. *J. Fluid Mech.* **121**, 403–424.

LONGUET-HIGGINS, M. S. 1992 Capillary rollers and bores. *J. Fluid Mech.* **240**, 659–679.

LÓPEZ, J., HERNÁNDEZ, J., GÓMEZ, P. & FAURA, F. 2005 An improved PLIC-VOF method for tracking thin fluid structures in incompressible two-phase flows. *J. Comput. Phys.* **208**, 51–74.

LUBIN, P. & GLOCKNER, S. 2015 Numerical simulations of three-dimensional plunging breaking waves: generation and evolution of aerated vortex filaments. *J. Fluid Mech.* **767**, 364–393.

MANSOUR, N. N., KIM, J. & MOIN, P. 1988 Reynolds-stress and dissipatio-rate budgets in a turbulent channel flow. *J. Fluid Mech.* **194**, 15–44.

MCLEAN, J. W., MA, Y. C., MARTIN, D. U., SAFFMAN, P. G. & YUEN, H. C. 1982 Three-dimensional instability of finite-amplitude water waves. *Phys. Rev. Lett.* **46** (13), 817–821.

MEI, C. C. 1983 *The Applied Dynamics of Ocean Surface Waves*. Wiley.

MELVILLE, W. K. 1982 The instability and breaking of deep-water waves. *J. Fluid Mech.* **115**, 165–185.

MELVILLE, W. K. 1996 The role of surface-wave breaking in air–sea interaction. *Annu. Rev. Fluid Mech.* **28**, 279–321.

MELVILLE, W. K., VERON, F. & WHITE, C. J. 2002 The velocity field under breaking waves: coherent structures and turbulence. *J. Fluid Mech.* **454**, 203–233.

MEZA, E., ZHANG, J. & SEYMOUR, R. J. 2000 Free-wave energy dissipation in experimental breaking waves. *J. Phys. Oceanogr.* **30**, 2404–2418.

MOON, I.-J., GINIS, I. & HARA, T. 2004 Effect of surface waves on air–sea momentum exchange. Part II: behavior of drag coefficient under tropical cyclones. *J. Atmos. Sci.* **61**, 2334–2348.

MUELLER, J. A. & VERON, F. 2009 Nonlinear formulation of the bulk surface stress over breaking waves: feedback mechanisms from air-flow separation. *Boundary-Layer Meteorol.* **130**, 117–134.

NEPF, H. M., WU, C. H. & CHAN, E. S. 1998 A comparison of two- and three-dimensional wave breaking. *J. Phys. Oceanogr.* **28**, 1496–1510.

https://doi.org/10.1017/jfm.2018.466 Published online by Cambridge University Press

NEW, A. L. 1983 A class of elliptical free-surface flows. *J. Fluid Mech.* **130**, 219–239.

OSHER, S. & SETHIAN, J. A. 1988 Fronts propagating with curvature-dependent speed: algorithms based on Hamilton–Jacobi formulations. *J. Comput. Phys.* **79**, 12–49.

PERLIN, M., CHOI, W. & TIAN, Z. 2013 Breaking waves in deep and intermediate waters. *Annu. Rev. Fluid Mech.* **45**, 115–145.

PERLIN, M., HE, J. & BERNAL, L. P. 1996 An experimental study of deep water plunging breakers. *Phys. Fluids* **8** (9), 2365–2374.

PERLIN, M., LIN, H. & TING, C.-L. 1993 On parasitic capillary waves generated by steep gravity waves: an experimental investigation with spatial and temporal measurements. *J. Fluid Mech.* **255**, 597–620.

PERLIN, M. & SCHULTZ, W. W. 2000 Capillary effects on surface waves. *Annu. Rev. Fluid Mech.* **32**, 241–274.

PIZZO, N. E., DEIKE, L. & MELVILLE, W. K. 2016 Current generation by deep-water breaking waves. *J. Fluid Mech.* **803**, 275–291.

POWELL, M. D., VICKERY, P. J. & REINHOLD, T. A. 2003 Reduced drag coefficient for high wind speeds in tropical cyclones. *Nature* **422**, 279–283.

QIAO, H. & DUNCAN, J. H. 2001 Gentle spilling breakers: crest flow-field evolution. *J. Fluid Mech.* **439**, 57–85.

RAPP, R. J. & MELVILLE, W. K. 1990 Laboratory measurements of deep-water breaking waves. *Proc. R. Soc. Lond.* A **331**, 735–800.

REUL, N., BRANGER, H. & GIOVANANGELI, J.-P. 1999 Air flow separation over unsteady breaking waves. *Phys. Fluids* **11** (7), 1959–1961.

REUL, N., BRANGER, H. & GIOVANANGELI, J.-P. 2008 Air flow structure over short-gravity breaking water waves. *Boundary-Layer Meteorol.* **126**, 477–505.

SCARDOVELLI, R. & ZALESKI, S. 1999 Direct numerical simulation of free-surface and interfacial flow. *Annu. Rev. Fluid Mech.* **31**, 567–603.

SCHULTZ, W. W., HUH, J. & GRIFFIN, O. M. 1994 Potential energy in steep and breaking waves. *J. Fluid Mech.* **278**, 201–228.

SHU, C.-W. & OSHER, S. 1989 Efficient implementation of essentially non-oscillatory shock-capturing schemes, II. *J. Comput. Phys.* **83**, 32–78.

SKYNER, D. 1996 A comparison of numerical predictions and experimental measurements of the internal kinematics of a deep-water plunging wave. *J. Fluid Mech.* **315**, 51–64.

SMITS, A. J., MCKEON, B. J. & MARUSIC, I. 2011 High-Reynolds number wall turbulence. *Annu. Rev. Fluid Mech.* **43**, 353–375.

SONG, C. & SIRVIENTE, A. I. 2004 A numerical study of breaking waves. *Phys. Fluids* **16** (7), 2649–2667.

SONG, J.-B. & BANNER, M. L. 2002 On determining the onset and strength of breaking for deep water waves. Part I: unforced irrotational wave groups. *J. Phys. Oceanogr.* **32**, 2541–2558.

STANSELL, P. & MACFARLANE, C. 2002 Experimental investigation of wave breaking criteria based on wave phase speeds. *J. Phys. Oceanogr.* **32**, 1269–1283.

SU, M.-Y., BERGIN, M., MARLER, P. & MYRICK, R. 1982 Experiments on nonlinear instabilities and evolution of steep gravity-wave trains. *J. Fluid Mech.* **124**, 45–72.

SULLIVAN, P. P., BANNER, M., MORISON, R. & PEIRSON, W. 2018 Turbulent flow over steep steady and unsteady waves under strong wind forcing. *J. Phys. Oceanogr.* **48**, 3–27.

SULLIVAN, P. P., MCWILLIAMS, J. C. & MOENG, C.-H. 2000 Simulation of turbulent flow over idealized water waves. *J. Fluid Mech.* **404**, 47–85.

SULLIVAN, P. P., MCWILLIAMS, J. C. & PATTON, E. G. 2014 Large-eddy simulation of marine atmospheric boundary layers above a specturm of moving waves. *J. Atmos. Sci.* **71**, 4001–4027.

SUSSMAN, M., FATEMI, E., SMEREKA, P. & OSHER, S. 1998 An improved level set method for incompressible two-phase flows. *Comput. Fluids* **27**, 663–680.

SUSSMAN, M. & PUCKETT, E. G. 2000 A coupled level set and volume-of-fluid method for computing 3D and axisymmetric incompressible two-phase flows. *J. Comput. Phys.* **162**, 301–337.

SUSSMAN, M., SMEREKA, P. & OSHER, S. 1994 A level set approach for computing solutions to incompressible two-phase flow. *J. Comput. Phys.* **114**, 146–159.

https://doi.org/10.1017/jfm.2018.466 Published online by Cambridge University Press

SUZUKI, N., HARA, T. & SULLIVAN, P. P. 2015 Impact of breaking wave form drag on near-surface turbulence and drag coefficient over young seas at high winds. *J. Phys. Oceanogr.* **43**, 324–343.

TAKAGAKI, N., KOMORI, S., SUZUKI, N., IWANO, K., KURAMOTO, T., SHIMADA, S., KUROSE, R. & TAKAHASHI, K. 2012 Strong correlation between the drag coefficient and the shape of the wind sea spectrum over a broad range of wind speeds. *Geophys. Res. Lett.* **39**, L23604.

TIAN, Z., PERLIN, M. & CHOI, W. 2008 Evaluation of a deep-water wave breaking criterion. *Phys. Fluids* **20** (6), 066604.

TIAN, Z., PERLIN, M. & CHOI, W. 2010 Energy dissipation in two-dimensional unsteady plunging breakers and an eddy viscosity model. *J. Fluid Mech.* **655**, 217–257.

TIAN, Z., PERLIN, M. & CHOI, W. 2012 An eddy viscosity model for two-dimensional breaking waves and its validation with laboratory experiments. *Phys. Fluids* **24**, 036601.

TOFFOLI, A., BABANIN, A., ONORATO, M. & WASEDA, T. 2010 Maximum steepness of oceanic waves: field and laboratory experiments. *Geophys. Res. Lett.* **37**, L05603.

TOWNSEND, A. A. 1980 *The Structure of Turbulent Shear Flow*. Cambridge University Press.

TROITSKAYA, Y. I., SERGEEV, D. A., KANDAUROV, A. A., BAIDAKOV, G. A., VDOVIN, M. A. & KAZAKOV, V. I. 2012 Laboratory and theoretical modeling of air–sea momentum transfer under severe wind conditions. *J. Geophys. Res.* **117**, C00J21.

TULIN, M. P. & WASEDA, T. 1999 Laboratory observations of wave group evolution, including breaking effects. *J. Fluid Mech.* **378**, 197–232.

VERON, F., SAXENA, G. & MISRA, S. K. 2007 Measurements of the viscous tangential stress in the airflow above wind waves. *Geophys. Res. Lett.* **34**, L19603.

WANG, Z., YANG, J. & STERN, F. 2016 High-fidelity simulations of bubble, droplet and spray formation in breaking waves. *J. Fluid Mech.* **792**, 307–327.

WEISSMAN, M. A. 1986 Observations and measurements of air flow over water waves. In *Wave Dynamics and Radio Probing of the Ocean Surface* (ed. O. M. Phillips & K. Hasselmann), chap. 23. Springer.

WEYMOUTH, G. D. & YUE, D. K.-P. 2010 Conservative volume-of-fluid method for free-surface simulations on Cartesian-grids. *J. Comput. Phys.* **229**, 2853–2865.

WU, C. H. & NEPF, H. M. 2002 Breaking criteria and energy losses for three-dimensional wave breaking. *J. Geophys. Res.* **107** (C10), 3177.

WU, C. H. & YAO, A. 2004 Laboratory measurements of limiting freak waves on currents. *J. Geophys. Res.* **109**, C12002.

YANG, D. & SHEN, L. 2010 Direct-simulation-based study of turbulent flow over various waving boundaries. *J. Fluid Mech.* **650**, 131–180.

YANG, Z., LU, X.-H., GUO, X., LIU, Y. & SHEN, L. 2017 Numerical simulation of sediment suspension and transport under plunging breaking waves. *Comput. Fluids* **158**, 57–71.

YAO, A. & WU, C. H. 2004 Energy dissipation of unsteady wave breaking on currents. *J. Phys. Oceanogr.* **34**, 2288–2304.

YAO, A. & WU, C. H. 2005 Incipient breaking of unsteady waves on sheared currents. *Phys. Fluids* **17**, 082104.

ZHANG, X. 1995 Capillary–gravity and capillary waves generated in a wind wave tank: observations and theories. *J. Fluid Mech.* **289**, 51–82.

ZHAO, Z.-K., LIU, C.-X., LI, Q., DAI, G.-F., SONG, Q.-T. & LV, W.-H. 2015 Typhoon air–sea drag coefficient in coastal regions. *J. Geophys. Res.* **120**, 716–727.

https://doi.org/10.1017/jfm.2018.466 Published online by Cambridge University Press